Title: Unsilenced inhibitory cortical ensemble gates remote memory retrieval

Authors: Shaoli Wang[1]†, Tao Sheng[1]†, Feng Su[4, 5, 6]†, He Yang[1] †, Rui Cao[7], Qiao Wang[7], Chen Zhang[4, 5]*, Wei Lu[1, 2, 3]*, #

Author Affiliations:

[1] Institute for Translational Brain Research, Department of Neurosurgery, Huashan Hospital, State Key Laboratory of Medical Neurobiology, Minister of Education (MOE) Frontiers Center for Brain Science, Fudan University, Shanghai 200032, China.

[2] MOE innovative Center for New Drug Development of Immune Inflammatory Diseases, Fudan University. China.

[3] MOE Key Laboratory of Developmental Genes and Human Disease, School of Life Science and Technology, Southeast University, Nanjing, Jiangsu Province 210096. China.

[4] Department of Neurobiology, School of Basic Medical Sciences, Beijing Key Laboratory of Neural Regeneration and Repair, Capital Medical University, Beijing, China

[5] Chinese Institute for Brain Research, Beijing, China

[6] Peking-Tsinghua Center for Life Sciences, Academy for Advanced Interdisciplinary Studies, Peking University, Beijing 100871, China.

[7] School of Information Science and Engineering and Yau Shing-Tung Center, Southeast University, Nanjing, 210096, China

† These authors contributed equally to this work.

*Correspondence should be addressed to: Dr. Wei Lu, Email: lu_wei@fudan.edu.cn; Dr. Chen Zhang, Email: czhang@ccmu.edu.cn

Lead contact: Dr. Wei Lu

Abstract

Acquired information can be consolidated to remote memory for storage but persists in a dormant state until its retrieval. However, it remains unknown how dormant memory is reactivated. Using a combination of simultaneous two-photon calcium imaging and holographic optogenetics in the anterior cingulate cortex (ACC) in vivo, we discover a subset of GABAergic neurons that are specifically associated with dormant memory retrieval. These interneurons display persistent activity and inter-neuronal synchronization at the remote memory stage. In the absence of natural contextual cues, directly activating these interneurons reliably recalls cortical ensembles relevant to remote memory retrieval with context specificity. Conversely, targeted volumetric inactivation of these neurons suppresses context-induced memory retrieval. Our results reveal an unexpected role of unsilenced inhibitory cortical ensembles in causally gating the retrievability of dormant remote memory.

Keywords: remote memory, memory retrieval, memory storage, anterior cingulate cortex, cortical ensemble

MAIN TEXT

Memories are thought to be initially encoded in the hippocampus (recent memory) but subsequently consolidated within the neocortex for permanent storage (remote memory) *(1-6)*. Accumulating evidence demonstrates that system consolidation transforms the labile and temporary memory trace to a mature and stable state in the cortex *(7-9)*. These memory traces undergo constant reorganization during system consolidation *(10, 11)* and may persist in a dormant state for years until being reactivated by encoding cues *(12-16)*.

To retain their functions in memory retrieval, memory traces should possess "retrieval handles" that permit activation by specific representations *(7, 17, 18)* Memory consolidation may enhance subsequent retrievability of the memory trace, consistent with the idea that "retrieval handles" are established after memory formation *(19)*. To date, however, it remains unknown how dormant traces are awakened for memory retrieval and whether such "retrieval handles" truly exist.

Here, to address this question, we focused on mesoscopic neuronal circuit activities in the anterior cingulate cortex (ACC). This region was found to be critically involved in remote memory storage and receives massive projections from other areas, such as the anterior thalamus, entorhinal cortex, and hippocampus *(20-24)*. Optogenetic manipulations revealed that these multi-region ACC afferents participate in the successful retrieval of multimodality associative memories *(25, 26)*. The ACC can thus act as an information integration and executive hub for coordinating memory traces. Via longitudinal tracking of neuronal calcium activities, we uncovered persistent activities and inter-neuronal synchronization among a small subset of GABAergic neurons. Via holographic single cellular optogenetic manipulations, we further demonstrated the causal role of inhibitory ensembles in gating remote memory retrieval.

Results

Unsilenced ACC neurons at the remote memory stage

We first set up a longitudinal two-photon imaging platform that enables simultaneous behavioral assays in live animals (Fig. 1A). We expressed a genetically encoded Ca^{2+} indicator (GCaMP6f, with viral tool rAAV2/9-hsyn-GCaMP6f) in the ACC (Fig. 1B, fig. S1, A and B, AP: 0.26 mm ML: -0.35 mm DV: 0.30 mm). The healthiness of these neurons subjected to long-term rAAV2/9 expression was validated (fig. S1, C to F). After a week of recuperation, mice were habituated to the head-fixed imaging platform for 3 weeks. Then, we subjected these mice to a contextual conditioning paradigm *(27, 28)* with properly adjusted parameters to induce remote memory formation *(29)*. The training session consisted of six trials with 40 seconds (s) of intertrial interval (ITI). In each trial, mice were consecutively presented with the virtual context composed of a 20 s baseline, 20 s of tone (2 kHz, 80 dB), and 18 s trace interval of silence, followed by a CO_2 laser nociceptive stimulus (20 ms, 8 W) (Fig. 1C). The fidget response was measured from pressure changes detected by a piezoelectric sensor located beneath the forepaws of restrained mice. Combined with video analysis, we ensured the specificity of the sensor for picked "fidgeting" behavior (fig. 2, A to E). After six trials, mice developed enhanced fidgeting responses to the contextual stimuli (fig. S2G). On the retrieval day (on day 63), mice were re-exposed to the conditioning context for the assessment of fidgeting behaviors for 3 minutes (min). We successfully trained mice to make an association between a virtual contextual cue and a fidget response induced

by nociceptive stimuli at the back paw. This associative memory was maintained and retrieved only on day 63 post-conditioning (Fig. 1D). As controls, mice trained with conditioning stimuli only (CS-only) or home-caged at all times failed to display fidgeting responses to the contextual stimuli.

We then tracked the neuronal activity dynamics via longitudinal two-photon calcium imaging through a cranial glass window above the ACC of awake, head-fixed mice (Fig. 1E). GCaMP6f signals of neurons at 200-300 μm depth were captured using a two-photon microscope at selected time points (*30*). To identify neuronal dynamics most relevant to remote memory, we focused on imaging data obtained 4-9 weeks (4-9 wks, 28-63 d) postconditioning. The two-photon sampling parameters were set at 30 Hz with a window size of 565×565 μm^2. The calcium transient for each identified neuron was quantified via analysis of the fluorescence change (ΔF/F) within the regions of interest (ROIs). Each ROI circled the somatic center of individual neurons on the all-time-point merged image. The overall neuronal activity level increased during conditioning and then decreased towards before-conditioning baseline level afterwards (Fig. 1F). During the entire 5 weeks of the remote stage we monitored, most neurons exhibited dynamic activities that fluctuated up and down the before conditioning baseline level. Nonetheless, we unexpectedly observed a small number (2~6) of neurons exhibited activities persistently above the baseline level (Fig. 1, F to H). These neurons displayed similar activity silencing after conditioning, but their activities could somehow be maintained at a modest level that persistently above the before-conditioning level and never dropped below the baseline at the entire remote stage, even though occasionally at some time points their activities were closed to the before-conditioning baseline. This observation was consistent across different subjects.

These incompletely silenced neurons drew our attention, as activated neurons during encoding have been proposed to enter a dormant state at the remote memory stage *(5, 23)*. To clarify this, we quantitatively assessed the elevated activities in these neurons via normalizing the changes in neuronal activity at each imaging time point, which was achieved by subtracting basal activity before conditioning. The normalized before conditioning neuronal activity was thus calculated as zero. For validation, we employed two independent but complementary approaches for analyses of calcium transients. We first calculated calcium power (Fig. 1I, Fig.1K1 and 1K2). By estimating the integrals of neuronal calcium spikes of all neurons*(31)* we revealed an early transient increase in averaged neuronal activities during conditioning, which declined dramatically to the before conditioning baseline level at the remote stage. We next applied spike inference analyses to the recorded calcium signals (Fig. 1J, Fig.1L1 and L2), which inferred the temporal occurrence of action potentials using a deep-learning-based method DeepSpike (for details see Methods) *(32)*. Both the two quantitative assessments uncovered a small subset of neurons with unique features on activity dynamics (Fig. 1K2 and 1L2). On one hand, these neurons displayed similar silencing of neuronal activity after conditioning. On the other hand, their spontaneous activities did not completely return to the baseline level. Instead, their activities were maintained at an intermediate level and further increased upon memory retrieval at 63 d (Fig. 1K and 1L; fig. S3). Therefore, the spontaneous activity level of these neurons did not reach the level for memory retrieval at the remote stage. Notably, the notion of persistent activity only applied to these neurons at the remote stage. At 30 min post-conditioning the unsilenced cells could still experience activities below baseline level (Fig. 1J).

We defined the neurons that maintained above-zero normalized calcium power for every imaging time point throughout the remote memory stages (28 d-63 d) as "unsilenced neurons" (see Methods for details on quantitative definition). Comparing neuronal activities at the remote stage in CS-US and CS-only group demonstrated that "unsilenced neurons" can only be identified in trained animals (fig. S4A to S4E). This was further corroborated by bootstrapping neuronal activities across time (fig. S4F to S4G).

To avoid false positive identification of these persistently active neurons as a result of inadequate sampling times, we calculated their percentage using different numbers of imaging time points. Our data show that when over 7 imaging time points were employed, the percentage of neurons with above-zero activity at the remote memory stage became relatively invariant (Fig. 1N and 1O).

As the targeted ACC region being imaged (AP: 0.26 mm ML: -0.35 mm DV: 0.30 mm; fig. S5A) is superficial and could be covered by the motor cortex, the above observations may correspond to the motor cortex. To rule out this possibility, we accurately pinpointed ACC in the imaging planes by employing the middle artery as a reference (fig. S5B and S5C) (*33*). All unsilenced neurons identified fell within perimeters of ACC in the imaging plane. Furthermore, we investigated the neuronal calcium dynamic across different imaging time points in the neighboring motor cortex. Based on the quantitative definition of unsilenced neurons, we did not detect any unsilenced neurons in the neighboring cortical region (fig. S5D), suggesting the unsilenced neurons we observed were indeed located in the surface ACC region.

Unsilenced ACC neurons are GABAergic

To further investigate the identity of the unsilenced neurons, we crossed *Viaat*-cre (Jackson Laboratory, strain No: 017535) mice with Ai9 mice (Jackson Laboratory, strain No: 007909) to obtain $GABA^{+/Cre}$;$Ai9^{wt/mut}$ (GABA-Cre::Ai9) mice, which express red fluorescence (mCherry) in GABAergic neurons in a Cre-recombinase-dependent manner (Fig. 2A) *(34)*. The GABAergic neuron labeling efficiency and specificity of mCherry expression in GABA::Ai9 mice were found to be 100% accurate with GAD67 staining (fig. S6)*(35)*. rAAV2/9-hsyn-GCaMP6f was then injected into the ACC of the transgenic mice for calcium imaging of all neurons. Longitudinal imaging revealed that all the unsilenced neurons exhibited both red fluorescence and GCaMP6f signals without exception (Fig. 2B and 2C). Unsilenced neurons were thus revealed to be entirely GABAergic (Fig. 2D). While memory traces have been principally classified as excitatory neuronal activities *(25)*, our finding that unsilenced neurons were exclusively GABAergic neurons is surprising and suggests actions of inhibition-induced excitation circuits in remote memory traces.

Unsilenced neurons maintain highly synchronized activity

Functionally correlated neurons can form neuronal ensembles for memory retrieval. To examine whether the unsilenced GABAergic neurons are functionally correlated, we assessed functional complex network formation based on the timing of calculated spontaneous calcium spikes in all GABAergic neurons *(24, 36)*. To reduce bias stemming from chance firings on the network structure, we employed a stringent deconvolution algorithm to derive the spike time series from raw calcium $\Delta F/F$ trace *(37)*. Furthermore, we normalized the synchronization counts at each imaging timepoint by subtracting randomized results from the actual values. Randomized samples were

generated by shuffling spike time series 10,000 times. Then, average synchronization counts of randomized firings were calculated and subtracted from the actual synchronization counts to obtain chance-firing corrected results. The calcium spikes were considered simultaneous firings only when they occurred at the same time (or precisely speaking, on the same captured frame) in any given imaging series. Pairwise synchronization was assessed between each pair of GABAergic neurons using a weighted adjacency matrix (Fig. 3A). Then, the inter-neuronal synchronized firing counts were graphed as a coactivity complex network. Basal connections partially existed occasionally between unsilenced neurons before training but were completely reconstructed or strengthened to a more stable, distinctive form during remote stages (Fig. 3B). Employing a combination of various additional analysis methods, we further demonstrated that elevated "synchronization" between unsilenced cells was not due to increased firing rates (please see fig. S7 and Methods).

When considering changes in synchronization in the population, we observed an overall increase in the average pairwise synchronization counts for all GABAergic neurons at the conditioning stage, followed by a rundown toward baseline levels at subsequent time points (Fig. 3C). Notably, high inter-neuronal synchronization between a small number (4 in shown sample) of GABAergic neurons was detected at the conditioning stage, which remained relatively stable throughout the remote memory stage (Fig. 3D and 3E). In contrast, synchrony analysis in non-GABAergic neurons failed to demonstrate similar observations (fig. S8A). Compared to GABAergic neurons, no distinct neuronal group could be separated in non-GABAergic neurons using unsupervised cluster analysis (fig. S8B). K-means clustering showed that the high synchronization neuronal group composed only of GABAergic neurons (fig. S8C), which indicated that the existence of high and low synchronization groups is a phenomenon specific to GABAergic neurons. More importantly, these neurons with inter-neuronal synchronization largely overlapped with the enduring unsilenced neurons (Fig. 3F), which were consistently observed for all subjects (Fig. 3, G and H). This overlap suggests that unsilenced neurons are highly intertwined GABAergic neurons. Their uniquely heightened and synchronized firing patterns may imply neural processes engaged in information maintenance.

To assess the stability of unsilenced neuronal activity patterns during the remote memory stage, we employed various cross-correlation assessments and information theory analyses. Firstly, we extracted topological structures based on synchronization patterns within the unsilenced neuron ensembles. We found that the network varied during conditioning and 30 min post-conditioning but transformed to a relatively stabilized state at the remote memory stage (fig. S9, A and B). Secondly, to assess stochasticity influence on the stable activity patterns, we calculated joint information entropy and joint mutual information based on information theory (fig. S9C) *(38-40)*. Again to correct for potential bias caused by chance firings, we calculated control entropy and mutual information values based on randomly shuffled data (fig. S9D, see Methods for details). Relative to randomized sample controls, unsilenced neuronal ensembles demonstrated a sustained decrease in average joint information entropy and an increase in average joint mutual information entering remote memory stages (fig. S9, E and F). Furthermore, decreased entropy was observed only in unsilenced neurons but not in the total GABAergic neuronal population or the entire imaged population (fig. S10). Lastly, we assessed unsilenced neuronal activity stability by calculating the Mahalanobis distance between all GABAergic neuronal activities at before-conditioning and remote memory time points *(41)*. Unsilenced neurons had the largest distance from the before conditioning

baseline at the remote stage (Fig. 9G), indicating their highly potentiated activities entering the remote stage. The above results collectively suggest a remarkable stabilization of functional networks within unsilenced neurons serving as potential substrates for remote memory retrieval.

Targeted activation of unsilenced neurons retrieved remote memory

To test whether activation of the enduring GABAergic cortical ensemble enables retrieval of remote memory, we performed simultaneous imaging and optogenetics via a holographic two-photon microscope equipped with lasers of two powers, one to image GCaMP6f (at 920 nm) and another to activate the redshifted opsin C1V1 (at 1,035 nm) *(42-44)*. For optogenetic manipulation, rAAV2/9-hsyn-C1V1(t/t) was injected at a depth of 200-300 μm into the ACC to express C1V1 in ACC neurons (Fig. 4A). We sequentially activated the selected unsilenced neurons via rapid movement of the galvo-galvo mirrors in a spiral manner. The time width of the optogenetics stimulation pulse is 2 seconds, and the illumination frequency within the pulse is 4 Hz. Stimulation quality tests showed robust depolarization in C1V1-expressing neurons without affecting the background control ROI (fig. S11, A and B). To further test the effect of stimulating the unsilenced neuronal ensemble, we also performed simultaneous stimulation with a spatial light modulator (SLM) that customizes beam split patterns (fig. S11C).

At 63 d after conditioning, all identified unsilenced neurons were simultaneously stimulated using 5 sweeps via SLM modules (Fig. 4B). The robustness and consistency of the holographic optogenetic activation were validated (see Methods for details). Targeted activation of these neurons not only increased fidgeting movements (Fig. 4C) but also rapidly evoked neuronal ensemble activation with considerable architectural similarity to that elicited by the conditioning context (Fig. 4D). To examine whether the reactivation of memory-like behavior is simply elicited by artificial stimulation of engram subpopulation, we compared between stimulation of unsilenced cells and stimulation of random memory-related GABAergic cells which is activated at the conditioning stage. For this purpose, we first defined those GABAergic cells with increased activities (1.3 folds of the baseline) during contextual conditioning as memory-related GABAergic neurons. Then we examined the effect of optogenetics stimulation of the same number of random GABAergic neurons. We found that random reactivation of the same number (2~6) of these memory-related GABAergic neurons, no matter at recent (2 days after conditioning) or remote time points, failed to induce similar memory-like behavior or ensemble activities (Fig. 4, C and D; fig. S12). Similar observations were obtained when the threshold to define memory-related cortical neurons changed to 50% activity increment (i.e., 1.5 folds of baseline). These results suggest that targeted reactivation of GABAergic cell subpopulation specific to unsilenced neurons gates memory retrieval at the remote stage.

We next examined the context specificity of the targeted unsilenced activation via successive conditioning of the animals to two different contexts at two specific time points (with 24-hour interval, Fig. 4, E and F). Based on the respective before-conditioning baselines, we subsequently validated the formation of two distinct context-specific subsets of “unsilenced neurons” (Fig. 4G). These results indicate that activation of these cortical neurons is sufficient to retrieve remote memory with context specificity.

Unsilenced neuron activation recalls cortical ensembles relevant to memory retrieval

To investigate whether the optically evoked cortical ensembles are relevant to memory retrieval, we assessed the degree of similarity between neuronal ensembles evoked by optogenetic and contextual stimuli. We extracted the entire neuronal ensembles responsive to stimuli immediately after stimulation (≤ 10 imaging frames) and analyzed their hierarchical structures by calculating the node and edge potential (*36,39*). We found that both forms of stimuli triggered neuronal ensembles with similar activation patterns and hierarchical structures, while random stimulation of memory-related GABAergic neurons activated at the conditioning stage only activated a small number of cells largely within 1 sampling point (33 ms) (fig. S12B) with sparse pattern totally different from that evoked by conditioning context (fig. S12C). The functional connection between these cells, measured in pairwise synchronization counts, is also weaker compared to the network under natural context recall (Fig. 5A-C; fig. S12D).

To quantitatively assess similarities between evoked ensembles, we calculated and compared cosine similarity, an index used to evaluate the difference between two different neural circuitry statuses *(42, 45, 46)*. The fluorescence signals were deconvoluted into binary sequences in the form of multidimensional vectors. Then the cosine of the angle between pairwise vectors in the multidimensional space was calculated. Finally, we normalized the inner products between each pair of neuronal ensemble population vectors to compare the similarity of the ensemble activity patterns under different stimuli (please see Methods for details). The results again confirmed that activity patterns triggered by conditioning context and targeted optogenetic stimulation were highly similar while differing from patterns induced by novel context (Fig. 5, D and E). This notion was further strengthened by our observations on two-context experiment. Targeted activation of the two context-specific subsets of "unsilenced cells" elicited distinct neuronal ensembles with similar architecture specific to their respective conditioning contexts (Fig. 5, F and G). In contrast, the similarity between the ensembles elicited by two different contexts was low (Fig. 5G). Thus, direct activation of the unsilenced neurons reactivates cortical ensembles relevant to the retrieval of specific remote memory.

To further validate the multilayer complex network, we conducted community analyses for ensemble activities under different retrieval conditions (fig. S13) *(47)*. Our results revealed that the unsilenced neurons, together with their downstream GABAergic and non-GABAergic neurons, constituted distinct layers of modules. Notably, the neuronal ensembles triggered by optogenetic stimuli showed similar modularity-class distributions to those triggered by conditioning context (fig. S12A). The modularity class distribution of topology evoked by novel context, however, significantly differed (fig. S12D). These results indicate that the functional modularity structures elicited upon unsilenced neuron activation were crucial to successful memory retrieval. The community analyses also revealed hierarchical modularity structures formed after unsilenced neuron activation during successful retrieval.

How can activating a small number of GABAergic inhibitory neurons evoke entire neuronal ensembles relevant to memory retrieval? One possibility is that the evoked neuronal ensemble constituted a small-world architecture under the control of unsilenced GABAergic neurons for the most efficient communication *(48, 49)*. Under this scheme, unsilenced GABAergic neurons serve as

a hub that exerts a maximal capacity to synchronously amplify the input signals via inhibition of other non-unsilenced GABAergic neurons *(50)*.

To identify the excitatory/inhibitory nature of the hierarchical responses, we examined neurons that responded within 10 imaging frames following the activation of unsilenced neurons (Fig. 5, H and I). We found most GABAergic neuronal responses were identified within 1 imaging frame (33 ms) following activation of unsilenced neurons during memory retrieval. Notably, these responsive GABAergic neurons displayed decreased activity (Fig. 5J). In contrast, non-GABAergic neurons with increased activity were largely observed at 99 ms sampling lag (Fig. 5K). This phenomenon hinted that targeted unsilenced neuron activation triggers downstream non-GABAergic neurons via a disinhibitory mechanism.

Unsilenced neuronal ensemble gates remote memory retrieval

To further investigate whether the inhibitory cortical ensemble constituted by unsilenced cells can gate the remote memory retrieval, we performed a loss-of-function experiment by targeted inactivation of unsilenced neurons in the imaging plane when the remote memory was retrieved by conditioning context at postconditioning day 63. rAAV2/9-hsyn-eNpHR3.0 was injected into the ACC region for this purpose. This manipulation elicited a minor tendency toward suppression of remote memory retrieval but was not statistically significant (fig. S14A). We speculate that remote memory retrieval may also engage unidentified unsilenced neurons in other imaging planes, which may account for the retrieval of remote memory under optogenetic inhibition.

To examine this possibility, we collaborate with microscopy engineers (Thorlabs, USA) to develop a technology that allows the delivery of simultaneous optogenetic manipulation on unsilenced neurons in three-dimensional (3D) space (in a volume of 565 × 565 × 180 μm^3, Figure 5H; see details in Methods). We found that the natural context indeed elicited the formation of unsilenced GABAergic neurons in other imaging planes (Fig. 6, A to C). Notably, three-dimensional (3D) volumetric optogenetic inhibition of unsilenced neurons in the whole imagining volume resulted in dramatic suppression of remote fear memory (Fig. 6D). In addition, the coactivity network of the entire ensemble was also visibly dampened post-inhibition (Fig. 6E). As a control, volumetric optogenetic inhibition of randomly selected neurons failed to exhibit similar effects (Fig. 6, E and F), highlighting the necessity of silencing a much larger number of unsilenced GABAergic cells for suppressing rather than activating memory retrieval. Furthermore, cosine similarity assessment of network activities revealed that conditioning context and 3D inhibition induce dissimilar patterns, and the same applied to novel context and 3D inhibition (Fig. 6, G and H). This corroborates former stimulation results and suggests that specific circuitry activity patterns underlie remote memory retrieval. Together, the above results suggest that a small number of unsilenced GABAergic neurons reliably gates cortical ensembles relevant to remote memory retrieval.

Discussion

Uncovering the trace for remote memory has always been a challenge in the field, as the memory traces activated during encoding subsequently undergo reorganization during consolidation and ultimately persist in a dormant state. To retain their potential for being retrieved, memory traces may possess “retrieval handles” that permit reactivation by specific representations *(7, 15, 19, 51)*.

Although these memory traces in a latent state comply with the brain's energy conservation principle, they also make memory reactivation difficult. The potential reorganization of memory traces further exacerbates this difficulty. Here, we reveal at the remote memory stage a small number of cortical GABAergic neurons that stably maintain elevated and synchronized activity. These neurons also displayed activity silencing after conditioning, but their activities never completely decreased to before-conditioning baseline level. Instead, they maintained their increased activities at a modest level above baseline throughout the remote stage. Despite being few in number, these cells can form a powerful and stable topology that is conducive to efficient information processing. The connectivity may function as a specialized “tag” for memory retrieval. Because of the elevated and synchronized activity, the tagged trace could be easily tracked down upon memory retrieval and thus may be employed as the “retrieval handle”. Our results with bidirectional targeted manipulations of the activity of these cortical neurons confirmed their causal role in gating the retrieval of remote memory. As the intermediate activity level of these unsilenced neurons remained substantially lower than that at the conditioning or retrieval stage, they failed to constantly recall the memory.

The cortical neurons we uncovered here for memory retrieval possess at least four characteristics. Firstly, they exhibited persistently higher activity compared to other neurons that enter dormant state. Despite a significant activity decrease since the memory encoding stage, they maintain an intermediate activity level above the before-conditioning baseline throughout the entire long-term memory stage. Secondly, the number of the unsilenced cortical neurons are stable. Thirdly, they displayed higher degree of inter-neuronal synchronization. The synchronous activity within these neurons implies the potential formation of a cohesive control unit that collaborates to perform retrieving functions. Fourthly, they all belong to GABAergic neurons in terms of their identity. Despite the limited population of these neurons, their activation as inhibitory interneurons enable them to exert control over a larger number of downstream neurons. The characteristics of these neurons place them in an intermediate critical state. While their own high activity is still not sufficient to trigger memory retrieval, the incoming external inputs can further activate them and thus facilitate this process.

What is the relationship between these unsilenced neurons and the conventional memory engram cells in the context of memory retrieval? Do they themselves belong to the population of engram cells? If so, engram cells themselves have tight networks and stimulation of engram subpopulation not just specific to unsilenced cells can also activates entire memory-related network. To address these questions, we compared stimulation of unsilenced cells and stimulation of random memory-related GABAergic cells activated at conditioning stage. We identified those GABAergic cells with increased activities during conditioning stage and then examined the effect of optogenetics stimulation of the same number of random GABAergic neurons. Random optogenetics stimulation of a small number of these memory-related GABAergic neurons at recent or remote stage failed to display any memory-like behavior. Furthermore, this stimulation only excited a small number of downstream cells with sparse pattern and weaker inter-neuronal pairwise synchronization. In contrast, reactivating unsilenced cells not only elicited memory-like behavior but also triggered a downstream hierarchical network with considerable similarity to the network elicited by conditioning context. These results suggest that the reactivation of memory-like behavior is not simply elicited by random stimulation of engram subpopulation, and targeted reactivation of

GABAergic cell subpopulation specific to unsilenced neurons gates memory retrieval at the remote stage, possibly via triggering downstream hierarchical network.

Our present findings point to the notion that memory consolidation helps to construct a pyramid-like multilayer structure *(52-57)*. This hierarchical structure, however, tends to be silent before retrieval. Using various network activity assessments and cross-condition comparisons, we revealed that successful memory retrieval reactivated this silent structure following the leading firings of unsilenced neurons. Furthermore, framewise coactivation analyses revealed that the closest following activated neurons were mostly GABAergic neurons, pointing to the possibility of reactivation of memory engrams through a disinhibitory mechanism *(58)*. It can be postulated that the unsilenced cortical ensembles enable the trigger of a "cascaded amplification" mechanism to effectively recall certain downstream neurons that function as latent traces for remote memory storage *(26, 59)*. Ensemble cosine similarity analyses on two distinctive contextual memories further revealed that retrieval was achieved by recalling hierarchical cortical ensembles with context specificity. The composition and multilayered structures of these evoked neuronal populations were similar under both contextual retrieval and artificial optogenetic retrieval. These results collectively show that contextual conditioning induces the formation or strengthening of enduring cortical ensembles at the remote memory stage, which are specialized for controlling the retrievability of latently stored remote memory traces.

While it may seem unconventional that a few cortical interneurons could activate specific behavioral responses, this phenomenon can be explained in several aspects. First, the observed context-specific hierarchical ensemble structures under successful memory retrieval indicate that unsilenced neurons act as “retrieval handles”. The cascaded downstream network response to unsilenced neuron activation may reflect the reactivation of dormant memory traces. Second, widespread brain state or behavioral changes induced by single-neuron stimulation have been observed in previous studies *(60-63)*. Granted, these studies mostly reported such effects in visual and somatosensory cortices. The observable behavioral changes induced by small neuronal ensemble stimulation nonetheless support the possibility of a cortical functional map at the cell population level (*53*). As the ACC serves as a primary associative cortical area integrating sensory and hippocampal inputs, sparse neuronal codes from upstream sensory areas could activate unsilenced neurons. The unsilenced neurons gate downstream remote memory traces likely via the disinhibitory multilayered network, maintaining their dormancy until being reactivated by corresponding sensory cues.

Although our findings suggest a multilayered network in gating remote memory retrieval, the functional and molecular details of this mechanism require further investigation. Future work could either aim to identify established GABAergic subtypes of unsilenced neurons or identify new molecular markers via single-cell sequencing techniques. The current results support functional connections between unsilenced neurons and downstream neuronal networks they control, which likely includes latent memory traces. By using more sensitive probes with higher spatial-temporal resolution, we would be able to examine the universalities of the gating mechanisms and further uncover the organization principles of the downstream memory trace in the mammalian brain.

REFERENCES AND NOTES

1. L. R. Squire, Mechanisms of memory. *Science* **232**, 1612-1619 (1986).

2. J. J. Kim, M. S. Fanselow, Modality-specific retrograde amnesia of fear. *Science* **256**, 675-677 (1992).

3. L. Nadel, M. Moscovitch, Memory consolidation, retrograde amnesia and the hippocampal complex. *Curr Opin Neurobiol* **7**, 217-227 (1997).

4. D. Tse *et al.*, Schemas and memory consolidation. *Science* **316**, 76-82 (2007).

5. S. Tonegawa, M. D. Morrissey, T. Kitamura, The role of engram cells in the systems consolidation of memory. *Nat Rev Neurosci* **19**, 485-498 (2018).

6. J. Kim, A. Joshi, L. Frank, K. Ganguly, Cortical-hippocampal coupling during manifold exploration in motor cortex. *Nature* **613**, 103-110 (2023).

7. Y. Dudai, The neurobiology of consolidations, or, how stable is the engram? *Annu Rev Psychol* **55**, 51-86 (2004).

8. Y. Dudai, A. Karni, J. Born, The Consolidation and Transformation of Memory. *Neuron* **88**, 20-32 (2015).

9. G. Doron *et al.*, Perirhinal input to neocortical layer 1 controls learning. *Science* **370**, (2020).

10. L. A. DeNardo *et al.*, Temporal evolution of cortical ensembles promoting remote memory retrieval. *Nat Neurosci* **22**, 460-469 (2019).

11. F. H. Do-Monte, K. Quinones-Laracuente, G. J. Quirk, A temporal shift in the circuits mediating retrieval of fear memory. *Nature* **519**, 460-463 (2015).

12. R. Semon, *The mneme*. (London : G. Allen & Unwin ltd.; New York : The Macmillan Company, [1921], 1921), pp. 304.

13. J. Najenson, What have we learned about the engram? *Synthese* **199**, 9581-9601 (2021).

14. P. W. Frankland, S. A. Josselyn, S. Kohler, The neurobiological foundation of memory retrieval. *Nat Neurosci* **22**, 1576-1585 (2019).

15. N. Yadav *et al.*, Prefrontal feature representations drive memory recall. *Nature* **608**, 153-160 (2022).

16. B. Lei, L. Lv, S. Hu, Y. Tang, Y. Zhong, Social experiences switch states of memory engrams through regulating hippocampal Rac1 activity. *Proc Natl Acad Sci U S A* **119**, e2116844119 (2022).

17. X. Sun *et al.*, Cortical preparatory activity indexes learned motor memories. *Nature* **602**, 274-279 (2022).

18. J. Minxha, R. Adolphs, S. Fusi, A. N. Mamelak, U. Rutishauser, Flexible recruitment of memory-based choice representations by the human medial frontal cortex. *Science* **368**, (2020).

19. S. A. Josselyn, S. Tonegawa, Memory engrams: Recalling the past and imagining the future. *Science* **367**, (2020).

20. S. A. Josselyn, S. Kohler, P. W. Frankland, Finding the engram. *Nat Rev Neurosci* **16**, 521-534 (2015).

21. S. Tonegawa, X. Liu, S. Ramirez, R. Redondo, Memory Engram Cells Have Come of Age. *Neuron* **87**, 918-931 (2015).

22. A. C. Toader *et al.*, Anteromedial thalamus gates the selection and stabilization of long-term memories. *Cell* **186**, 1369-1381 e1317 (2023).

23. P. W. Frankland, B. Bontempi, L. E. Talton, L. Kaczmarek, A. J. Silva, The involvement of the anterior cingulate cortex in remote contextual fear memory. *Science* **304**, 881-883 (2004).

24. B. Bontempi, C. Laurent-Demir, C. Destrade, R. Jaffard, Time-dependent reorganization of brain circuitry underlying long-term memory storage. *Nature* **400**, 671-675 (1999).

25. X. Liu *et al.*, Optogenetic stimulation of a hippocampal engram activates fear memory recall. *Nature* **484**, 381-385 (2012).

26. P. Rajasethupathy *et al.*, Projections from neocortex mediate top-down control of memory retrieval. *Nature* **526**, 653-659 (2015).

27. S. F. Cooke, R. W. Komorowski, E. S. Kaplan, J. P. Gavornik, M. F. Bear, Visual recognition memory, manifested as long-term habituation, requires synaptic plasticity in V1. *Nat Neurosci* **18**, 262-271 (2015).

28. Y. Tian *et al.*, An Excitatory Neural Assembly Encodes Short-Term Memory in the Prefrontal Cortex. *Cell Rep* **22**, 1734-1744 (2018).

29. I. Goshen *et al.*, Dynamics of retrieval strategies for remote memories. *Cell* **147**, 678-689 (2011).

30. X. Pang *et al.*, Gallic Acid Ameliorates Cognitive Impairment Caused by Sleep Deprivation through Antioxidant Effect. *Experimental Neurobiology* **32**, 285-301 (2023).

31. C. L. Wee *et al.*, A bidirectional network for appetite control in larval zebrafish. *Elife* **8**, (2019).

32. A. Speiser *et al.*, paper presented at the NIPS 2017, 2017.

33. R. Huda *et al.*, Distinct prefrontal top-down circuits differentially modulate sensorimotor behavior. *Nat Commun* **11**, 6007 (2020).

34. H. T. Chao *et al.*, Dysfunction in GABA signalling mediates autism-like stereotypies and Rett syndrome phenotypes. *Nature* **468**, 263-269 (2010).

35. D. L. Kaufman, C. R. Houser, A. J. Tobin, Two forms of the gamma-aminobutyric acid synthetic enzyme glutamate decarboxylase have distinct intraneuronal distributions and cofactor interactions. *J Neurochem* **56**, 720-723 (1991).

36. E. Schneidman, M. J. Berry, 2nd, R. Segev, W. Bialek, Weak pairwise correlations imply strongly correlated network states in a neural population. *Nature* **440**, 1007-1012 (2006).

37. E. A. Pnevmatikakis *et al.*, Simultaneous Denoising, Deconvolution, and Demixing of Calcium Imaging Data. *Neuron* **89**, 285-299 (2016).

38. N. M. Timme, C. Lapish, A Tutorial for Information Theory in Neuroscience. *eNeuro* **5**, (2018).

39. E. D. Fagerholm *et al.*, Cortical Entropy, Mutual Information and Scale-Free Dynamics in Waking Mice. *Cereb Cortex* **26**, 3945-3952 (2016).

40. C. W. Yuan, C. Leibold, Recurrent coupling improves discrimination of temporal spike patterns. *Front Comput Neurosci* **6**, 25 (2012).

41. K. Ghandour *et al.*, Orchestrated ensemble activities constitute a hippocampal memory engram. *Nat Commun* **10**, 2637 (2019).

42. L. Carrillo-Reid, S. Han, W. Yang, A. Akrouh, R. Yuste, Controlling Visually Guided Behavior by Holographic Recalling of Cortical Ensembles. *Cell* **178**, 447-457 e445 (2019).

43. A. M. Packer, L. E. Russell, H. W. Dalgleish, M. Hausser, Simultaneous all-optical manipulation and recording of neural circuit activity with cellular resolution in vivo. *Nat Methods* **12**, 140-146 (2015).

44. L. Carrillo-Reid *et al.*, Identification of Pattern Completion Neurons in Neuronal Ensembles Using Probabilistic Graphical Models. *J Neurosci* **41**, 8577-8588 (2021).

45. W. Yang, R. Yuste, Holographic imaging and photostimulation of neural activity. *Curr Opin Neurobiol* **50**, 211-221 (2018).

46. L. Carrillo-Reid, W. Yang, J. E. Kang Miller, D. S. Peterka, R. Yuste, Imaging and Optically Manipulating Neuronal Ensembles. *Annu Rev Biophys* **46**, 271-293 (2017).

47. D. Meunier, R. Lambiotte, E. T. Bullmore, Modular and hierarchically modular organization of brain networks. *Front Neurosci* **4**, 200 (2010).

48. E. Bullmore, O. Sporns, The economy of brain network organization. *Nat Rev Neurosci* **13**, 336-349 (2012).

49. K. M. Igarashi, L. Lu, L. L. Colgin, M. B. Moser, E. I. Moser, Coordination of entorhinal-hippocampal ensemble activity during associative learning. *Nature* **510**, 143-147 (2014).

50. F. Donato, S. B. Rompani, P. Caroni, Parvalbumin-expressing basket-cell network plasticity induced by experience regulates adult learning. *Nature* **504**, 272-276 (2013).

51. J. Yokose *et al.*, Overlapping memory trace indispensable for linking, but not recalling, individual memories. *Science* **355**, 398-403 (2017).

52. E. Tulving, Z. Pearlstone, Availability versus accessibility of information in memory for words. *Journal of Verbal Learning and Verbal Behavior* **5**, 381-391 (1966).

53. M. P. van den Heuvel, O. Sporns, Rich-club organization of the human connectome. *J Neurosci* **31**, 15775-15786 (2011).

54. G. Zamora-Lopez, C. Zhou, J. Kurths, Exploring brain function from anatomical connectivity. *Front Neurosci* **5**, 83 (2011).

55. G. Zamora-Lopez, C. Zhou, J. Kurths, Graph analysis of cortical networks reveals complex anatomical communication substrate. *Chaos* **19**, 015117 (2009).

56. T. Geiller *et al.*, Local circuit amplification of spatial selectivity in the hippocampus. *Nature* **601**, 105-109 (2022).

57. L. Luo, Architectures of neuronal circuits. *Science* **373**, eabg7285 (2021).

58. K. M. Hagihara *et al.*, Intercalated amygdala clusters orchestrate a switch in fear state. *Nature* **594**, 403-407 (2021).

59. T. J. Ryan, D. S. Roy, M. Pignatelli, A. Arons, S. Tonegawa, Memory. Engram cells retain memory under retrograde amnesia. *Science* **348**, 1007-1013 (2015).

60. C. D. Meliza, Y. Dan, Receptive-field modification in rat visual cortex induced by paired visual stimulation and single-cell spiking. *Neuron* **49**, 183-189 (2006).

61. C. Y. Li, M. M. Poo, Y. Dan, Burst spiking of a single cortical neuron modifies global brain state. *Science* **324**, 643-646 (2009).

62. A. C. Kwan, Y. Dan, Dissection of cortical microcircuits by single-neuron stimulation in vivo. *Curr Biol* **22**, 1459-1467 (2012).

63. A. R. Houweling, M. Brecht, Behavioural report of single neuron stimulation in somatosensory cortex. *Nature* **451**, 65-68 (2008).

64. Y. Shymkiv, R. Yuste, Aberration-free holographic microscope for simultaneous imaging and stimulation of neuronal populations. *Opt Express* **31**, 33461-33474 (2023).

65. K. Juczewski, J. A. Koussa, A. J. Kesner, J. O. Lee, D. M. Lovinger, Stress and behavioral correlates in the head-fixed method: stress measurements, habituation dynamics, locomotion, and motor-skill learning in mice. *Sci Rep* **10**, 12245 (2020).

66. F. Su, Y. Tian, Non-rigid Registration for Two-photon Imaging Using Triangulation and Piecewise Affine Transformation. *Neuroscience* **491**, 1-12 (2022).

67. M. Li, F. Liu, H. Jiang, T. S. Lee, S. Tang, Long-Term Two-Photon Imaging in Awake Macaque Monkey. *Neuron* **93**, 1049-1057 e1043 (2017).

68. L. Carrillo-Reid *et al.*, Encoding network states by striatal cell assemblies. *J Neurophysiol* **99**, 1435-1450 (2008).

ACKNOWLEDGEMENTS

We thank Dr. Lu-Yang Wang, Dr. Wei-Qun Fang, Dr. Peng Yuan and all members of the Lu lab for discussion and support.

Funding:
The Science Technology Innovation 2030 Project of China (2021ZD0203502 to WL)
The National Natural Science Foundation of China (T2394531 to WL)
The Ministry of Science and Technology of China (2021YFA1101302 to WL)
The National Natural Science Foundation of China (32200835 to SLW)
The China Postdoctoral Science Foundation (2021M700847 to SLW).

AUTHOR CONTRIBUTIONS

Investigation: SW, TS, FS, HY, RC
Supervision: WL, CZ
Funding Acquisition: WL
Visualization: SW, TS
Writing: WL, SW, HY

DECLARATION OF INTERESTS

The authors declare no competing interests.

INCLUSION AND DIVERSITY

We support inclusive, diverse, and equitable conduct of research.

RESOURCE AVAILABILITY

Lead contact

Further information and requests for reagents and resources should be directed to W. Lu (lu_wei@fudan.edu.cn).

Material availability

This study did not generate new unique reagents.

Data and code availability

- All data and analyses necessary to understand and assess the conclusions of the manuscript are presented in the main text and in the supplementary materials.
- All the analysis codes are available from the lead contact upon request.

Figures and Figure Legends

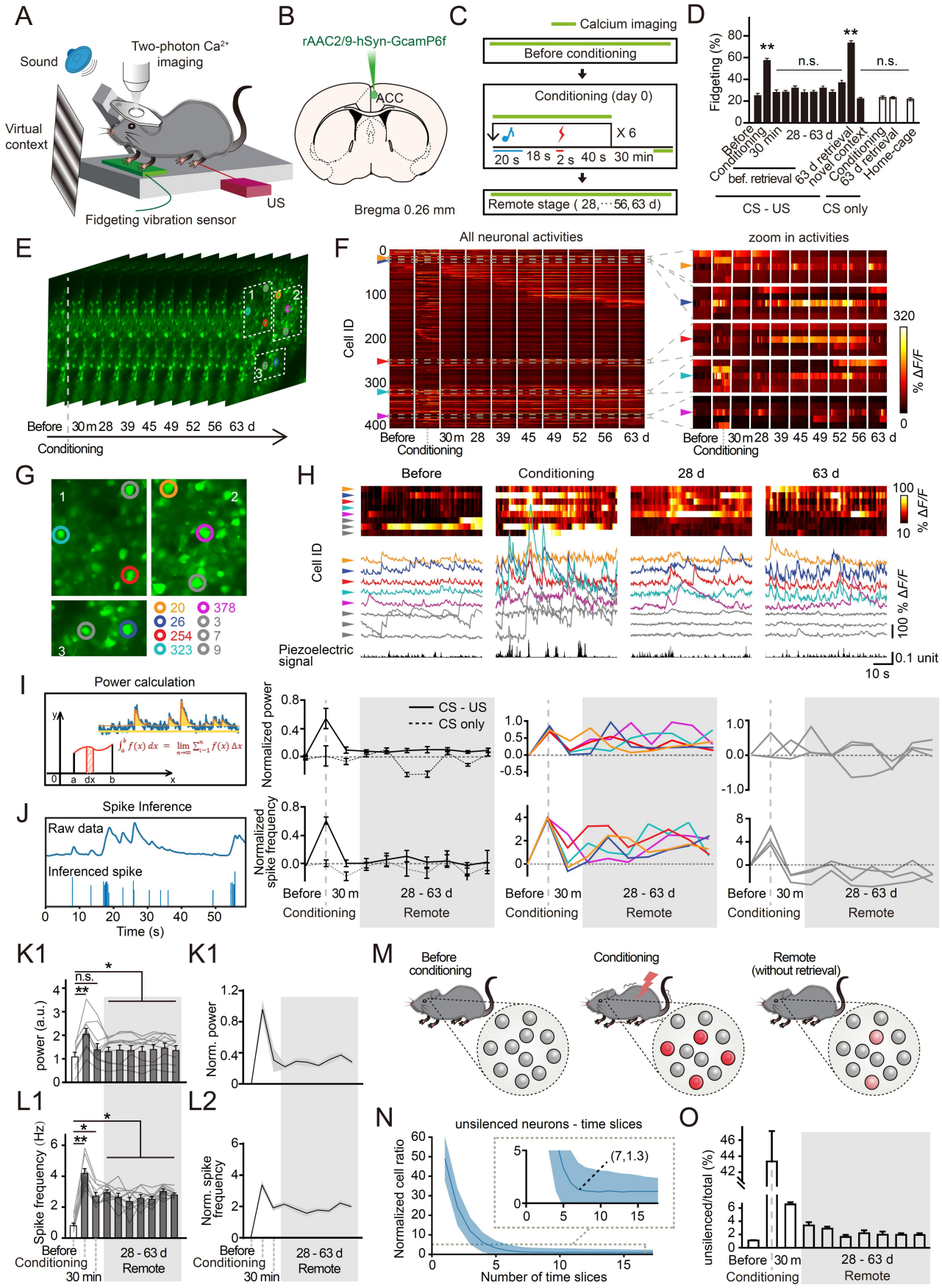
A
Sound
Two-photon Ca2+ imaging
Virtual context
US
Fidgeting vibration sensor
B
rAAC2/9-hSyn-GcamP6f
ACC
Bregma 0.26 mm
C
Calcium imaging
Before conditioning
Conditioning (day 0)
X 6
20 s 18 s 2 s 40 s 30 min
Remote stage (28,···56, 63 d)
D
Fidgeting (%)
n.s.
Before Conditioning
30 min
28 - 63 d
bef. retrieval
63 d retrieval
novel context
Conditioning
63 d retrieval
Home-cage
CS - US
CS only
E
Before 30 m 28 39 45 49 52 56 63 d
Conditioning
F
All neuronal activities
zoom in activities
Cell ID
% ΔF/F
G
20
26
254
323
378
3
7
9
H
Before
Conditioning
28 d
63 d
Cell ID
% ΔF/F
Piezoelectric signal
0.1 unit
10 s
I
Power calculation
Normalized power
CS - US
CS only
J
Spike Inference
Raw data
Inferenced spike
Time (s)
Normalized spike frequency
Before Conditioning
30 m
28 - 63 d
Remote
K1
power (a.u.)
Norm. power
L1
Spike frequency (Hz)
L2
Norm. spike frequency
30 min
M
Before conditioning
Conditioning
Remote (without retrieval)
N
unsilenced neurons - time slices
Normalized cell ratio
(7,1.3)
Number of time slices
O
unsilenced/total (%)

Figure 1. A small number of unsilenced neurons are identified at remote memory stages. (A) Schematic diagram showing the contextual conditioning setup under a two-photon microscope. US, unconditioned stimuli. **(B)** rAAV2/9-hsyn-GCaMP6f injection site at the ACC (AP: 0.26 mm, ML: -0.35 mm, DV: 0.30 mm). **(C)** Experimental protocols and imaging timeline. **(D)** Successful formation and retrieval of context (conditioned stimuli, CS) foot shock (unconditioned stimuli, US) associative memory. The CS-US group showed a significantly higher fidgeting response during remote memory retrieval (day 63) compared to all other time points (without retrieval), $P < 0.0001$. CS-only and home-caged controls showed no changes, $P > 0.1$, one-way ANOVA with Tukey's post hoc test, $*P < 0.05$, $**P < 0.01$, mean ± s.e.m. Conditioning data were from the last trial of conditioning as in all the following figures. "Before" in the plot refers to before conditioning. **(E)** Schematic diagram of two-photon images at a depth of 200-300 μm. Colored circles mark 5 neurons with persistently increased activities above the before-conditioning level. Each color denotes cellular ID, consistent in all following figures G-J. Gray circles mark 3 randomly selected neighboring neurons with activities fluctuating around the baseline. **(F)** Heatmaps showing calcium transients (ΔF/F) from all identified neurons within the imaging field at different imaging time points. Right, zoomed-in images in dotted lined boxes on the left. Among all the detected neurons, 5 of them (ID marked by arrow colors) exhibited persistently increased activities at the remote memory stage (post-conditioning day 28-63). The color bar indicates ΔF/F values. n = 405 neurons from 1 animal. **(G)** Zoomed-in two-photon images (all time points averaged) numbered according to dotted lined boxes in E. The colored numbers at lower right corner refer to cell ID marked by colored arrows in F. **(H)** Temporally aligned activity heatmap (top), raw calcium traces of selective neurons (middle), and fidgeting response (bottom) obtained at different time points. **(I)** Sustained increase in unsilenced neurons during the entire remote memory stage revealed by calcium power analysis. The diagram at left shows the power calculation methods. The line charts at right show temporal changes in normalized neuronal calcium power in all neurons (black line), in unsilenced neurons (colored line), or in randomly selected neighboring neurons (grey line). The dotted line at zero indicates the normalized before-conditioning baseline. The shaded portions indicate the remote memory stage. Normalization was performed by subtracting the average calcium power of the before-training baseline from the average power of each time point. **(J)** Neuronal spike counts based on spiking activity inference algorithms identified the same unsilenced neurons. The diagram shows reconstructed neuronal calcium spikes obtained by the deep learning method DeepSpike. Calibration bar: 5 s, 40% ΔF/F. The arrangement of line charts matched those in panel I. **(K, L)** Bar graph shows increased remote stage graphs reveal a modestly elevated calcium power (K) and spike frequencies (L) were maintained in unsilenced neurons at remote stage (K1, before vs. cond. $P < 0.001$; before vs. remote, $P < 0.05$; L1, before vs. cond. $P < 0.01$, before vs. 30 min, $P < 0.05$, before vs. remote, $P < 0.01$, each timepoint's value was compared to Before's value using nonparametric Friedman test with Dunn's correction for multiple comparisons, n = 52 neurons from 12 animals). K1 and L1 show non-normalized values; K2 and L2 show values normalized by subtracting data from the before imaging timepoint. These unsilenced neurons displayed similar silencing of neuronal activity after conditioning. However, their activities did not return to before-conditioning baseline level. Instead, they maintained their activities at a modest level above baseline throughout the remote stage. Power a.u., power in arbitrary unit (a.u.). Gray area covers remote time points. **(M)** The diagram illustrating the neuronal activity evolvement across different stages. Note at remote stage the spontaneous activity of unsilenced neurons does not return to

baseline level. Instead, it maintains in an intermediately potentiated state. The weight of red color denotes the neuronal activity level. **(N)** Influence of the number of imaging time points on unsilenced neuron identification. When the number of imaging time points (time slices) exceeded 7, the normalized number of active neurons became stabilized (4.33 ± 0.22, n = 12 animals; ratio over total neuronal number shown in the magnification box), justifying our inclusion of 7 remote-stage imaging time points to delineate unsilenced neurons. **(O)** Temporal changes in the percentage of unsilenced neurons in all animals. The percentage peaked at the conditioning stage, then decreased and finally stabilized at 1.60 ± 0.24% on day 63 (n = 12) of the remote memory stage.

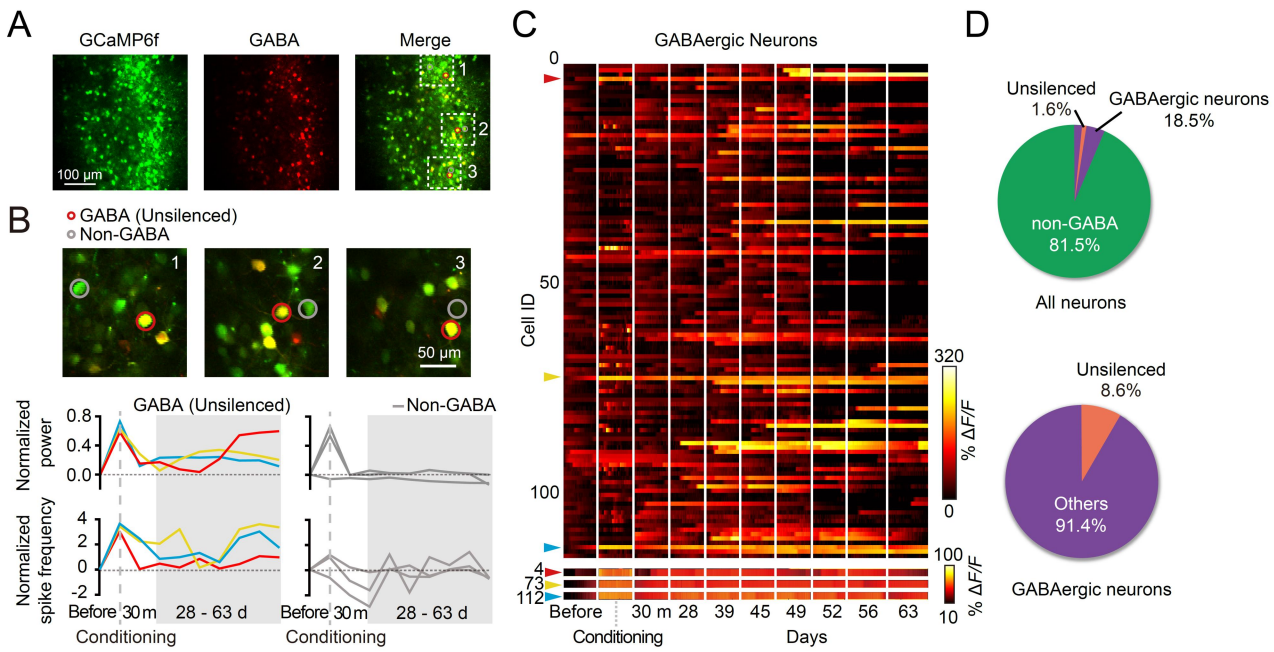

Figure 2. Unsilenced neurons are GABAergic. (A) Sample image (all time points averaged) in GABA::Ai9 mice. The left image refers to all GCaMP6f-labeled cells in the imaging field. GABAergic neurons were those labeled by mCherry signals (middle). In merged image (right) neurons in yellow refer to co-labeled GABAergic neurons. Dotted line boxes illustrate the location of unsilenced neurons (circled in red). **(B)** Magnified images marked by dotted line boxes in a. Fig. 2a demonstrate that unsilenced neurons are GABAergic. The unsilenced neurons (circled in red; top), which maintained increased activity at the remote stage (post-conditioning day 28-63), both in terms of both normalized calcium power (middle) and DeepSpike inferred spike frequencies (grey line; bottom) at the remote stage (post-conditioning day 28-63), were all identified as GABAergic neurons in yellow. Neighboring non-GABAergic neurons (circled in gray) were employed as the control. **(C)** Heatmaps of neuronal activities of all GABAergic neurons recorded across different time points. The unsilenced neurons maintain increased activity during the entire remote stage. Arrow colors marked cell ID corresponding to B. Color bar shows ΔF/F value. **(D)** Pie chart showing a low percentage of unsilenced cells in all imaged neurons and in all GABAergic neurons. The percentage of unsilenced neurons was calculated by dividing the count of unsilenced neurons by the total number of all GCaMP+ neurons.

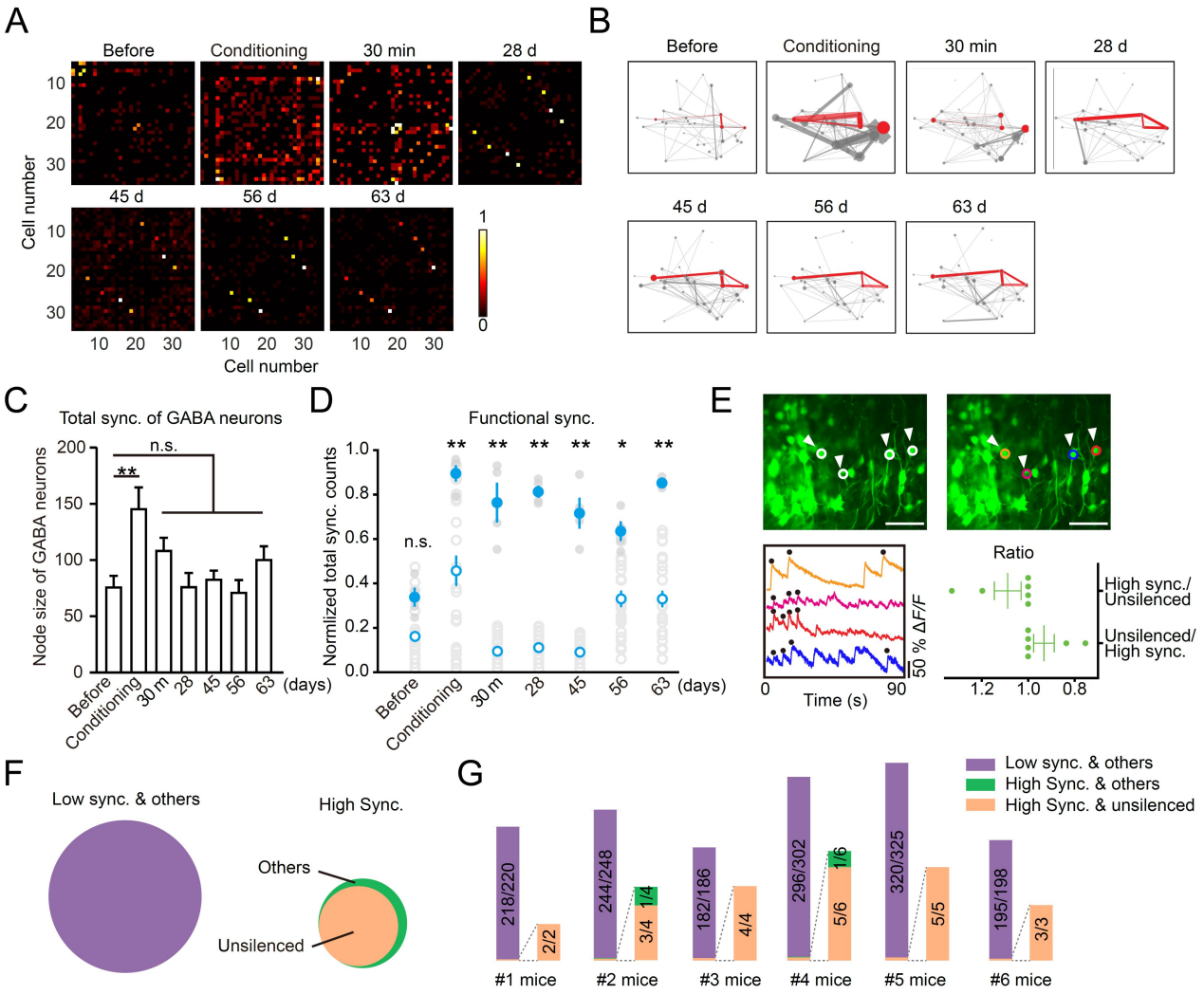

Figure 3. Unsilenced neurons maintain a high synchronization level. (A) Pairwise synchronization counts between all GABAergic neurons mirrored along the diagonal line. Values were calculated from the temporal cooccurrence of neuronal spikes inferred by the deconvolution algorithm (see Methods). An overall increase in pairwise correlations was detected during the last trial of conditioning, followed by a rundown toward the baseline level. In contrast, heightened pairwise synchronization was maintained between a few GABAergic neurons. **(B)** Coactivity complex network of neurons in Fig. 3A. Each node position corresponds to the actual neuronal location in the imaging field. Red, unsilenced neurons; gray, other neurons. The thickness of the line positively correlates to the synchronization counts between the two neurons that it connects. The size of the node positively correlates to the sum of pairwise synchronization counts between that neuron and all other neurons. At the remote memory stage (post-conditioning day 28-63), node size for unsilenced neurons decreased, while their inter-neuronal edge size increased. This indicates that instead of maintaining nonselective interactions with all other neurons, unsilenced neurons mostly synchronize with each other at the remote memory stage. **(C)** Pairwise synchronization within all GABAergic neurons increased during conditioning and decreased toward the before-training level at the remote memory stage. The node size of GABA neurons refers to the total synchronization counts from all GABAergic neurons. Conditioning vs Before: $P < 0.01$, one-way ANOVA with Tukey's post hoc test, $*P < 0.05$, $**P < 0.01$, n = 5 animals. **(D)** Pairwise synchronization counts

yielded two distinct neuronal populations with high synchronization (high sync; counts ≥ 3σ, filled circles) and low synchronization (low sync; counts < 3σ, empty circles) *$P < 0.05$, **$P < 0.01$, n = 4 neurons for high sync. neurons, n=31 neurons for low sync. neurons in 1 animal. **(E)** Highly matched neuron identity between unsilenced and high sync neurons. neurons. Top, representative two-photon images of high sync. neurons (white circle, left) and unsilenced neurons (colored circle, right). Bottom left, calcium traces of neurons circled in top right images. Trace colors match with the top right image. Black dots mark calcium spikes (threshold: $\Delta F/F \geq 2\sigma$) that synchronize with those of other traces. Bottom right, count ratio of high sync. neurons and unsilenced neurons. (unsilenced/high sync. 0.93 ± 0.05, high sync/unsilenced 1.09 ± 0.06, n=6). **(F)** Venn diagram of unsilenced neurons and high sync. neurons. Unsilenced neurons (GABAergic) made up most of the high sync. neurons. Others refer to cells with calcium power that fluctuate or drop below baseline activities during remote stages. **(G)** Distribution of the numbers of unsilenced and high sync. neurons across different subjects.

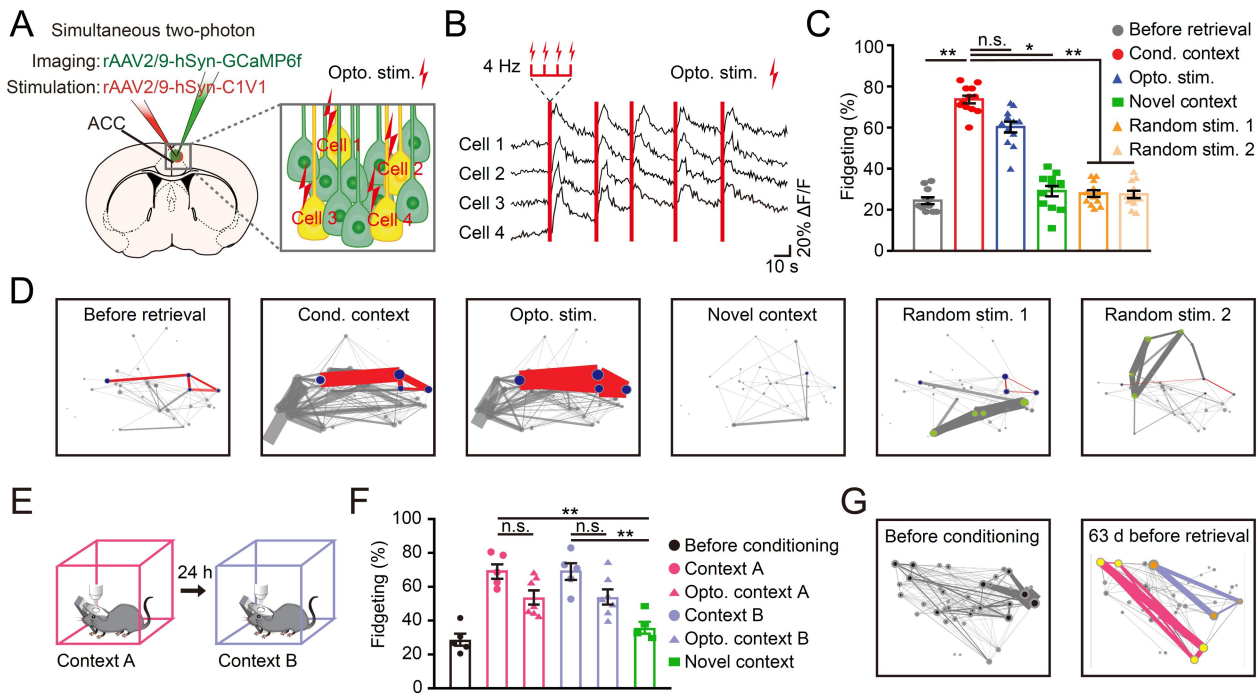

Figure 4. Holographic stimulation of unsilenced neurons retrieves remote memories with context specificity. (A) Experimental schematics and viral injection site. Single-cell resolution stimulation was achieved via either a spatial light modulator (SLM) or rapid movement of the galvo-galvo mirrors (right). **(B)** Validation of holographic stimulation. Holographic stimulation evoked robust and repeatable activations calcium transients in randomly selected test neurons. The inset shows stimulation paradigm. The time width of the optogenetic stimulation pulse is 2 seconds, and the illumination frequency within the pulse is 4 Hz. To better test the stimulation efficacy, the optogenetic stimuli were delivered with unfixed interval. For the retrieval experiment, however, each stimulation was delivered 5 times at 10 s apart. **(C)** Successful remote memory retrieval by optogenetic stimulation of unsilenced neurons. Optogenetic stimulation elicited a similar fidgeting rate to that induced by conditioning contextual stimulation (P = 0.125 > 0.05; n = 12, one-way ANOVA with Tukey's post hoc test, mean ± s.e.m.). In contrast, the novel context or stimulation of the same number of randomly selected neurons elicited a much lower fidgeting rate (Random stim1 vs. Before retrieval, P = 0.766 > 0.05, Random stim2 vs. Before retrieval, P = 0.839 > 0.05, Random stim1 vs. Novel context, P > 0.05, Random stim2 vs. Novel context, P = 0.999 > 0.05; n=12, one-way ANOVA with Tukey's post hoc test, mean ± s.e.m.). **(D)** Similar coactivity network patterns upon optogenetic and conditioning contextual memory retrieval. As the control, novel contextual cues or stimulation of randomly selected GABAergic neurons elicit completely different coactivity patterns. Node color semantics: blue, unsilenced neurons; green, randomly stimulated GABAergic neurons. Red wedges denote pairwise synchronization between unsilenced neurons. For node and wedge calculations, see Fig. 3B. **(E)** Two-context experimental design. **(F)** Successful retrieval of remote memories by optogenetic stimulation of unsilenced neurons corresponding to their respective contexts (Context A vs. Bef., P < 0.01; Context B vs. Bef., P < 0.01; Opto. context A vs. Bef., P < 0.01; Opto. context B vs. Bef., P < 0.01, one-way ANOVA with Tukey's post hoc test, n = 7 animals, mean ± s.e.m.). Optogenetic stimulation of each of the two subsets of unsilenced neurons elicited similar fidgeting responses as their corresponding conditioning contexts, indicating that targeted activation of these cortical neurons is sufficient to retrieve remote memory (Context A

vs. Novel context, $P < 0.01$, Opto. context A vs. Novel context, $P = 0.006 < 0.01$; Context B vs. Novel context, $P < 0.01$, Opto. Context B vs. Novel context, $P = 0.005 < 0.01$, one-way ANOVA with Tukey's post hoc test, n = 7 animals, mean ± s.e.m.). **(G)** Coactivity network patterns depict the formation of two context-specific subsets of unsilenced neurons. Each subset of unsilenced neurons was determined by checking whether calcium power was persistently above their respective before-training baseline activities for every remote-stage imaging time point. Distinct subsets of unsilenced neurons (marked by yellow and orange) correspond to the two contexts (pink for context A and purple for context B).

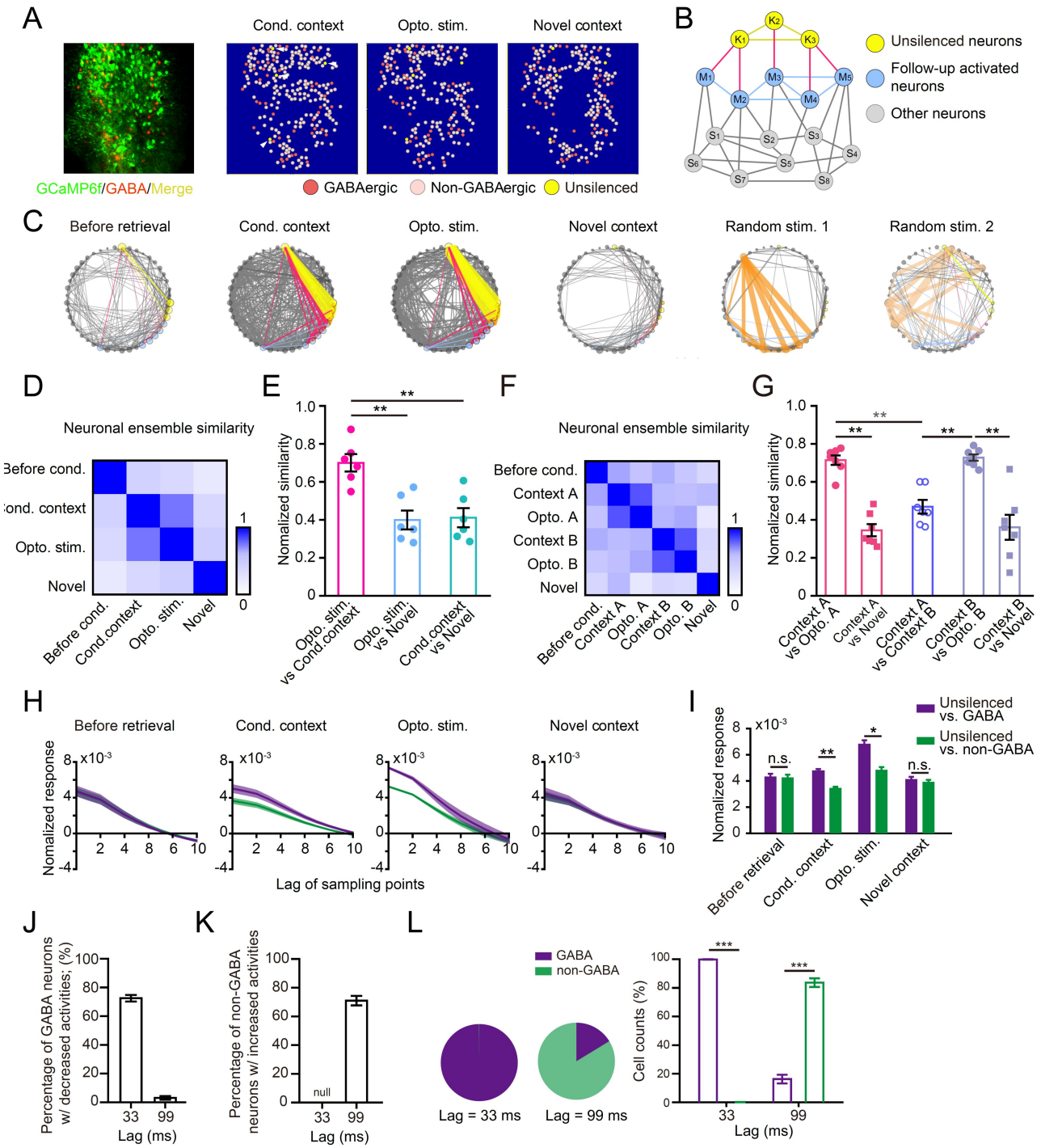

Figure 5. Unsilenced neuron activation recalls hierarchical functional networks relevant to memory retrieval. (A) Ensemble patterns (displayed by dot distribution) under contextual recall and optogenetic stimulation were similar compared to those under novel context. Left, two-photon images averaged from all time points. Right, diagrams of neurons activated upon memory retrieval under various conditions. **(B)** Hierarchical structures of elicited neuronal topological structure. Yellow, unsilenced neurons; blue, follow-up activated neurons within 1 sampling point (33 ms) after unsilenced neuron activation; gray, all other neurons. **(C)** Similar topological structural dynamics were observed under cond. context and optogenetic stimulation. As the control, neither novel context nor random GABAergic neuron stimulation exhibited similar effects. Color semantics

match B. Orange, randomly selected GABAergic neurons. **(D)** Average cosine similarity of population activities under different stimuli in 1 animal. The highest ensemble similarity was found for optogenetic stim. and cond. context. **(E)** Normalized average cosine similarity confirmed the highest similarity between ensemble activities under opto. stim. and cond. context (70.66 ± 4.61, $P < 0.01$ compared to cond. and novel context similarity, $P < 0.01$, n = 6 animals, one-way ANOVA with Tukey's post hoc test, mean ± s.e.m.). **(F)** Targeted activation of the two context-specific subsets of "unsilenced cells" elicited distinct neuronal ensembles with similar architecture specific to their respective conditioning contexts. **(G)** Normalized average cosine similarity analysis confirmed the high similarity between the neuronal ensembles elicited by Opto. stimulations and their respective contexts (Context A vs. Opto. A vs. Context A vs. Novel context, P < 0.01; Context A vs. Opto. A vs. Context A vs. Context B, P = 0.0009 < 0.01). In contrast, the similarity was low between neuronal ensembles elicited by two different contexts (context B vs. Opto. B vs. Context A vs. Context B, P = 0.0004 < 0.01, n = 7 animals, one-way ANOVA with Tukey's post hoc test, mean ± s.e.m.), supporting that context-specific memories are represented by distinctive ensemble patterns in the ACC. **(H)** GABAergic neurons preferentially responded to unsilenced neuron stimulation. Mean ± s.e.m. Lag of sampling points denotes the number of frames (33 ms per frame) following unsilenced neuron stimulation. Normalized responses (Y axis) calculate the normalized number of neurons (separated into GABAergic and non-GABAergic groups) that responded to unsilenced neuron activation. Normalization is performed by taking the ratio between each value and the mean. Color scheme illustrated in I. **(I)** Average follow-up responses to unsilenced neurons confirmed the priority of GABAergic neuron responses following unsilenced neurons during memory retrieval. Under cond. context, more GABAergic neurons responded to unsilenced neuron activation ($P = 0.004 < 0.01$), likewise for Opto. stim. ($P = 0.0104 < 0.05$, n = 40 neurons from 5 animals, unpaired t-test, mean ± s.e.m.). **(J, K)** Most GABAergic neurons responsive to unsilenced neuron activation were identified in the sampling lag within 33ms and displayed decreased activity (J). In contrast, non-GABAergic neurons with increased activity were largely observed at 99 ms sampling lag (J). **(L)** The percentage distribution of GABA or non-GABAergic cells following activation of unsilenced neurons. Lag = 33 ms, GABA (99.87 ± 0.13) vs. non-GABA (0.13 ± 0.13), P < 0.01; Lag = 99 ms, GABA (16.29 ± 3.03) vs. non-GABA (83.71 ± 3.03), P < 0.01, paired t-test. Non-GABAergic neurons fired in lag (mostly in 99 ms) compared to GABAergic neurons, suggesting a disinhibitory network downstream of unsilenced neurons.

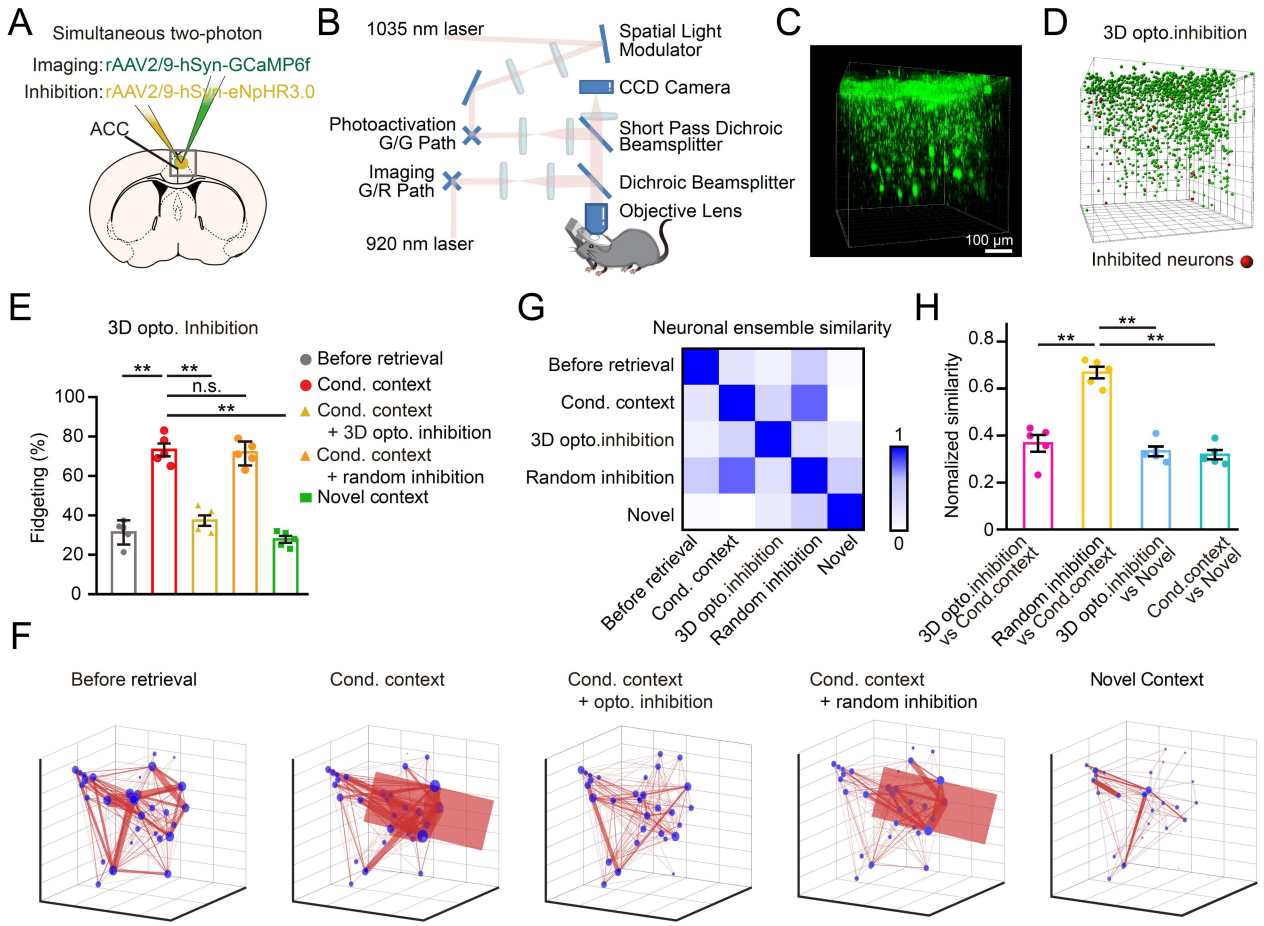

Figure 6. Targeted 3D holographic inhibition of unsilenced neurons impairs remote memory retrieval. (A) 3D holographic optogenetic inhibition setup. Volumetric imaging was achieved via piezoelectric modules at 3Hz sampling rate. Stimulation was achieved via SLM. **(B)** Schematics of microscope setup. Two ultrafast lasers combined with galvo/resonant (G/R) and galvo/galvo (G/G) paths were employed respectively for imaging and spatial light modulator stimulation. **(C, D)** 3D reconstruction diagram of the entire imaged neuronal population in a volume of 565×565×180 μm^3. n = 1611 neurons in 1 animal. Inhibited unsilenced neurons are marked in red in D (n = 43 neurons). **(E)** Successful suppression of remote memory retrieval via volumetric targeted inactivation of unsilenced neurons. Under the conditioning context, inhibition of unsilenced neurons reduced the fidgeting rate to a level comparable to novel context control (Cond. Context vs. before retrieval, $P < 0.01$, Cond. Context + 3D opto. inhibition vs. before retrieval, $P = 0.454 > 0.05$). In contrast, inhibition of randomly selected GABAergic cells did not reduce fidgeting (Cond. Context + random inhibition vs. before retrieval, $P < 0.01$, Cond. Context +3D opto. inhibition vs. Cond. context, $P < 0.01$, one-way ANOVA with Tukey's post hoc test, n = 5 animals, mean ± s.e.m.). **(F)** 3D coactivity network patterns demonstrate suppression of pairwise neuronal synchronization by volumetric inhibition of unsilenced neurons. Only unsilenced neurons are shown. **(G)** Cosine similarity analysis revealed that targeted 3D inhibition of unsilenced neurons decreased the ensemble similarity to that elicited by Cond. Context. **(H)** Normalized average cosine similarity confirms lower similarity in 3D opto. inhibition vs Cond. context compared to Random inhibition/Cond. context.

Supplementary Materials

Materials and Methods

Animals

All animal procedures were performed under the guidelines of the Institutional Animal Care and Use Committee of Fudan University. Wild-type C57BL/6 male mice were purchased from GemPharmatech (Nanjing, China) and Vital River Laboratories (Beijing, China). To distinguish GABAergic and non-GABAergic neurons, *Vigat*-cre (Jackson Laboratory, strain No: 017535) were crossed with Ai9 mice (Jackson Laboratory, strain No: 007909) to obtain $GABA^{+/Cre}$::$Ai9^{wt/mut}$ (GABA-Cre::Ai9) mice. Genotypes were determined via PCR postnatally at 21 days. All mice were group housed in five at the SPF facility of the Department of Laboratory Animal Science at Fudan University. Animals were maintained on a 12-hour reverse light-dark cycle with *ad libitum* access to water and a chow diet. All experiments were performed during the light cycle of mouse subjects. All mice were aged 2-5 months old at the time of viral injection. The number of subjects in each treatment group was determined based on expected variance and effect size from previous imaging and behavioral studies.

Stereotactic and head plate attachment procedure

Before surgery, the mice (4 weeks of age) were anesthetized with tribromoethanol by intraperitoneal (i.p.) injection (240mg/kg, Sigma-Aldrich, USA). Local anesthesia and post-operational pain management were given by lidocaine hydrochloride gel (Xinya Med Co., China) applied to the skin around the incision. A thin layer of erythromycin eye ointment (Baijingyu Med Co., China) was applied to the eyes for protection. Body temperature was maintained at 37 °C with a small heating pad. The target surface of the mouse skull was exposed with a ring incision after shaving the head. The periosteum over the exposed skull surface was removed using a scalpel and hydrogen peroxide (3%). The location of ACC region (AP 0.26 mm; ML -0.35 mm; DV 0.3 mm) was then determined via the standard stereotactic procedure and a cranial window (5×5 mm^2 size) was opened directly above the targeted region followed by viral injections.

For optogenetic stimulation, a cocktail of viruses rAAV2/9-hsyn-GCaMP6f-WPRE (500 nl, 2e12 vg/ml) and rAAV2/9-hsyn-C1V1(T/T)-TS-P2A-WPRE (500 nl, 2e12 vg/ml) were injected into ACC region (AP 0.26 mm; ML -0.35 mm; DV 0.3 mm) using pulled glass pipettes. For optogenetic inhibition, C1V1 was replaced for rAAV2/9-hsyn- eNpHR3.0-(T/T)-TS-P2A-WPRE (500 nl, 2e12 vg/ml). The injection rate was set at 30 nL/min, and the pipette was held for 15 min post injection to avoid fluid flow back due to pipette removal. A 5-mm circular glass coverslip was placed and sealed by cyanoacrylate adhesive for chronic imaging.

After the cranial window was closed by the glass coverslip, a custom-designed titanium head plate was attached to the skull by dental cement (Yuyan Instruments, China). Postsurgical dexamethasone sodium phosphate (2 mg/kg, Shanxi Ruicheng Kelong Veterinary Medicine Co., Ltd. China) and ceftriaxone sodium (200 mg/kg, Guangxi Kelun Pharmaceutical Co., Ltd. China) were respectively injected subcutaneously and intraperitoneally daily for a week. During this period mice recuperated in the home cage with food and water *ad libitum*. Ceftriaxone sodium was also injected daily for 12 weeks during the entire experiment to prevent inflammation.

Two-photon imaging protocol

The imaging system employed in our study was Thorlabs' Bergamo® II Series Multiphoton Microscope (Thorlabs, USA). For two-photon imaging, the Coherent Chameleon Vision II (Coherent Corp. USA) Ti:Sapphire Laser (920 nm) was employed as the laser source coupled with an 8kHz Galvo/Resonant (G/R) scanner. For optogenetic stimulation and inhibition, the Coherent Monaco 1035 nm femtosecond laser was used to excite red-shift opsins C1V1 or eNpHR3.0, coupled with a Galvo/Galvo (G/G) scanner. Simultaneous imaging and holographic optogenetic manipulation were thus achieved respectively via the G/R and the G/G path. The laser power, stimulation positions, and patterns were quality-controlled by their corresponding commercial software (ThorImage 4.1, USA).

At each data acquisition time point, mice were awake and head-fixed on the platform. To realize effective longitudinal tracking of the same group of neurons, reference brightfield images of the cortical surface and two-photon images of the targeted area were acquired for each animal during "before-training" baseline recordings. In all subsequent imaging, hardware coordinates were checked and representative features (blood vessels and each neuron) within the imaging window were manually re-aligned with the reference image. Images were acquired at 30 Hz for 90s (2800 frames) at each imaging time point. 16 × objective, 0.8 NA, Nikon object lens was employed. The field of view (FOV) was set at 512 × 512 pixels (565 × 565 μm^2). The laser power was strictly monitored for an average value smaller than 80 mW across all sessions to reduce phototoxicity and bleaching.

3D volumetric imaging was achieved via fast-scan piezoelectric modules. The module controlled the movement of the objective lens in a 400 μm range via voltage-dependent deformation. During 3D imaging, the focal plane was moved vertically at 20 μm per step upon complete acquisition of one 2D imaging plane (fig. S5 below). The 20 μm step length was determined based on the average soma size of cortical neurons (19.1 μm) to minimize inter-neuronal signal interference along the z-axis. The average soma size was measured from 400 randomly selected neurons in 2 animals under 3D scan. Each imaging plane consisting of 512×512 pixels (565 × 565 μm^2) was acquired via the Galvo/Resonant scanner in a raster pattern, moving in the two-way scan mode. A total of 10 planes were obtained to construct a 3D FOV of 565 × 565 × 180 μm^3. For each animal, the deepest imaging plane with clearly visible neurons was selected as the sampling start point. The sampling starting depth ranged from 560-500 μm and the ending depth ranged from 380-320 μm below the pia surface. Each imaging plane costed 33 ms (at 30 Hz sampling rate) to complete. The effective sampling rate was 3 Hz. The time dwelt on each 3D field of view (FOV) was 330 ms.

As ACC is mostly covered by neighboring motor cortex, we took two measures in ACC targeted imaging experiments to corroborate the region-specificity. First, we referred to the previous study and employed the middle artery as a reference for positioning.(*33*) Second, we replicated the exact same imaging experiments in the motor cortex (AP:0.26 mm, ML:-0.7, DV:0.3 mm) lateralized to targeted ACC area. Based on the quantitative definition for unsilenced neurons, we did not detect any unsilenced neurons in neighboring cortical regions, suggesting no unsilenced neurons could be identified in the motor cortex. The unsilenced neurons we observed were thus indeed located in surface ACC region.

Holographic optogenetics protocol

Holographic imaging and stimulation were conducted using the commercial Bergmo II microscope (Thorlabs, USA) installed with a volumetric spatial light modulator (SLM) module. In-vivo holographic stimulation was first performed sequentially as quality control and then simultaneously for the formal experiment. Sequential stimulation mode employed the spiral scan feature of the Galvo/Galvo scanner (A1R MP+, Nikon). Simultaneous holographic stimulation was achieved via the SLM module established in collaboration with Thorlabs. The light path was established based on designs by Yuste et al. (*64*) and more detailed information could be obtained from Thorlabs (https://www.thorlabs.com/) upon request. Two laser oscillators were integrated respectively to the imaging (Coherent Chameleon Vision II with 80 MHz pulse freq., 140fs pulse width used at 920 nm) and stimulation (Coherent Monaco with 80 MHz pulse freq., < 400fs pulse width fixed at 1035 nm) light paths of the Thorlabs Bergmo II microscope. The SLM window was also separated into two regions for simultaneous modulation of imaging and stimulation paths lasers. For beam width registration of the two imaging and stimulation lasers to their assigned SLM regions beam-expanding telescopes were employed following the pockels cells. To rule out interference from the two regions we employed spatial filters (SF) in conjugated pupil planes and a zero-order block (ZOB) for removal of zero-order beam. The entire holographic control volume approximately covered $600 \times 600 \times 400\ \mu m^3$.

The diameter of stimulation ROIs was set to be consistent with the observed averaged cell body size. The laser power was set at 5-20 mW on each neuron. The specific power of the optical stimulation was analyzed and examined via commercial software (ThorLabs, USA). Activation effects for both sequential and SLM stimulation were tested first on a fluorescent plate and then in vivo (fig. S9). Pre-stimulation SLM calibration was performed via the commercial coupled software (ThorLabs). The calibration software automatically computes the transformation between SLM target coordinates and imaging FOV coordinates on the burnt locations on the fluorescence plate using methods described previously.

For results reported in Fig. 5D and L, all identified co-active neurons were simultaneously stimulated using five sweeps via SLM modules (Thorlab, USA). Stimulation frequency is 4Hz and each sweep lasts 2 seconds. Animals (n = 3) that did not show full response ($\Delta F/F > 3\sigma$) to all sweeps were excluded. In the remaining 12 animals, 10 animals successfully retrieved remote memories upon target activation of unsilenced neurons. The stimulation success rate of 100 % per sweep and average response of 0.69 ± 0.15 (norm. $\Delta F/F$) is comparable to previous literature.(*43*)

For the random stimulation results reported in Fig. 5D and L and fig. S11, stimulation targets were selected in the following steps. First, all identified GABAergic neurons in the imaging plane were given a number ID. Then a fixed number of IDs were randomly selected as stimulation targets. The number of IDs selected was determined by the number of identified unsilenced neurons in that subject (for specific numbers please see supplementary tables).

All optogenetic manipulations were delivered on day 63 thirty minutes post memory retrieval tasks. To assess the causal role of unsilenced neurons in memory retrieval, a total 3 min of 3D optogenetic inhibition was delivered on selected unsilenced neurons accompanied by training context (context A) presentation. Inhibition was separated into two trials (1.5 min each, with 2 min ITI within) to limit thermal damage on the neurons.

Behavioral assays

The behavioral paradigm was adapted from the classical contextual fear conditioning task which consists of a training block under context A and day 63 retrieval tasks under context A, a novel context B and optogenetic manipulation-induced artificial retrieval. We used a mini-computer (Raspberry Pi) controlled tablet screen to display the virtual context to the animal at the start of each trial. During training trials, the screen displayed a room corner furnished with wooden floors and square-shaped wall decoration; during novel context trials, the screen displayed photos of a living room furnished with gray floors, dark walls, and white sofas. For optogenetic stimulation, the screen was turned off, and the animal was kept in a default dark environment.

A week post viral injection, each animal was placed on a head-restraint apparatus under the two-photon microscope for 30 - 60 min daily (for a total of 21 days) to reduce restraint brought-on anxiety and stress and adapt to the experimental environment during the imaging process.(*65*) On the first day, the mice were exposed to the training environment for 3 min without any stimulations before the conditioning training. Then the virtual context (conditioned stimulation, CS) was delivered and the tone stimuli were set at 2 kHz, 80 dB for 20 s by an audio controller. Nociceptive stimuli (unconditioned stimulation, US) were delivered via the DM-300 CO_2 laser stimulator (20 ms, 8 W; custom designed by Dimei Optics & Electronics Tech. Co. Changchun, Jilin, China) attached to the animal's back paw. The training session contained six consecutive training blocks with an ITI of 40 s, each training block consists of a 20 s baseline, a 20 s, 80 dB tone, followed by an 18 s trace interval of silence and a 20 ms, 8 W nociceptive foot shock. On the retrieval day, mice were re-exposed to the conditioning context to assess contextual conditioned fidgeting behavior for 3 min. Then after 30 min rest, mice were exposed to a novel virtual context for 3 min as the control. 3 min after the onset of novel context presentation, mice were also presented with the 20s tone CS, and demonstrated increased fidgeting during tone presentation (53.2% vs. 29.2% before tone CS presentation, please see fig. S13A).

For the two-context test, each animal first underwent the entire training session under context A and then 24 h later under context B. On the retrieval day, mice were re-exposed to context A and 24h later to context B. On retrieval test day 3, mice were presented with a novel context C to assess the contextual specificity of the associative memory. The novel context C consists of two rooms, one furnished with gray floors, blue walls, and pink sofas and one furnished with wooden floors, green walls, and green sofas.

Control experiments were performed to test if the formation of unsilenced neurons relies on tone presentation. Animals were conditioned without tone (spatial context+ nociceptive laser) and presented the conditioning context during retrieval sessions. On the training day, animals were exposed successively to context A and context B. The order in which we present the two contexts was counterbalanced across animals. Context A consists of square building blocks with metal floors. Context B consists of triangular building blocks with coarse cardboard floors. For each trial, a 2 s, 1mA foot shock was administered 38s upon context presentation. 6 trials were repeated with an intertrial interval of 30 s. On the retrieval day, context A, context B, and a novel context were successively presented, each for 3 min. The order of presentation was again counterbalanced across animals. The novel context consists of irregular quadrilateral building blocks with metal floors. Our results demonstrated that animals successfully formed memories respectively for context A and

context B (fig. S13B). The behavioral performance during 63 d memory tests, however, was inevitably weakened compared to training with tone. Collectively, our results show that the formation of unsilenced neurons and the retrieval of remote memory is independent on tone stimuli.

To test if the formation of unsilenced neurons were influenced by the head-fixed paradigm, we also replicated the entire assay in standard fear conditioning box. Animals were first habituated to the imaging platform for 21 days and then trained in a classical fear conditioning box. Fear conditioning was carried out in the default background (grid floor, plexiglass walls), consisting of 6 trials of 20 s, 8 kHz tone, 18 s trace delay, and 2 s, 1 mA foot shocks. The intertrial interval was 30 s. After training, animals were imaged at selective time points (30 min, 28 d - 63 d). Mice successfully formed associative memories under this paradigm (fig. S13B), with an overall decrease in freezing compared to fidgeting on the imaging platform. Our new data demonstrated that unsilenced cells can still be identified under the free-moving training paradigm, indicating that they are not a phenomenon specific to the head-fixed fidgeting behavioral assays.

Experimental designs are illustrated in Figures 1A to C. The movement of the animal's forepaws was recorded as a change in the continuous voltage signals being recorded throughout the entire experiment. All the virtual context cues, sound cues, pain delivery, fidgeting movements, and imaging acquisition were controlled by the EPC-10 amplifier (Heka, Germany) to synchronize delivery and recording.

Fidgeting rate analysis

The fidgeting rate was measured from voltage changes in a piezoelectric sensor positioned under the animal's forepaws. Absolute value of raw signals from the piezoelectric sensor was plotted in Fig. 1H. For fidgeting behavior analysis(*27, 28*), the recorded continuous voltage signal was down-sampled to 100 Hz, and then the average voltage throughout the entire recording time was calculated as F0. Relative changes in signals were calculated by (F-F0)/F0. To eliminate negative values, the amount of fidgeting was calculated by taking the root mean square of the voltage signal. To quantify behavior associated with conditioning, the average fidgeting rate 3 min before training was calculated as the baseline, and the percent time of fidgeting movement above 3 standard deviations (SD) from the baseline was calculated for each experiment session.

To validate the results on fidgeting behavior, we employed video analysis to assess the specificity of the sensor for picked "fidgeting" behavior. Specifically, we trained the animal under head-fixed conditions in a conditioning box under the exact same protocol used in previous experiments. Then we video-recorded the entire behavioral assay on the imaging platform and analyzed the grip and release motion of the animal's front paw. Each grip of the animal's front paw was labeled as a "fidgeting" response via frame-to-frame comparison analysis, which we termed video-analyzed fidgeting (V.A. fidgeting). The V.A. fidgeting index calculated the degree of motion (frame-to-frame difference) in the video and small V.A. fidgeting values correspond to front paw gripping (similar to "freezing" in classical fear conditioning video analysis). The gripping actions increased front paw pressure, as captured by increases in raw piezoelectric signals. Therefore, small V.A. fidgeting values correspond to animals' conditioned fidgeting response, whereas large raw piezoelectric signals correspond to fidgeting behavior (fig. S2A). The exact inverse relationship between V.A. fidgeting and piezoelectric trace shown in Figure A demonstrated a good match in

results from these two methods. We calculated the matching rate of V.A. fidgeting responses and the piezo-electric recorded signals as 77.56% (fig. S2C). From this value, we obtained a mismatching rate of 22.44% (100%-77.56%). To further assess whether the 22.44% mismatching rate would cause bias in behavioral tests, we generated 1000 simulated fidgeting responses at baseline and remote stages (in a range of true values ± 22.44%). We conducted t-tests using these simulated values and found that 99.6% of p-values were significant (<0.05, fig. S2D and S2E). Since the original t-test based on true fidgeting values was also significant (<0.05), this result indicated that the conclusion of animals significantly responding to conditioned stimuli during remote retrieval remained the same no matter for simulated or true results. The small chances of mismatch between piezoelectric signals and V.A. fidgeting could not override the conclusion on remote memory retrieval. Together these results suggest that the signals-labeled "fidgeting" response could be used as a reliable readout for the behavioral expression of memory.

To further examine if other behavioral changes that would corroborate our findings with fidgeting, we employed the fear conditioning protocol (e.g. freely moving tone fear conditioning followed by 2P imaging) to see if they can elicit activation of ACC excitatory neurons. Animals were first habituated to the imaging platform for 21 days and then trained in a classical fear conditioning box. Fear conditioning was carried out in the default background (grid floor, plexiglass walls), consisting of 6 trials of 20 s, 8 kHz tone, 18 s trace delay, and 2 s, 1 mA foot shocks. The intertrial interval was 30 s. After training, animals were imaged at selective time points (30 min, 28 d - 63 d). Mice successfully formed associative memories under this paradigm (fig. S2F), with an overall decrease in freezing compared to fidgeting on the imaging platform. Our preliminary results demonstrated that unsilenced cells can still be identified under free-moving training paradigm, indicating that they are not a phenomenon specific to the head-fixed fidgeting behavioral assays. Together, these results suggest that the signals-labeled "fidgeting" response could be used as a reliable readout for the behavioral expression of memory.

Image data processing

Image processing was performed with ImageJ (National Institutes of Health, Bethesda, MD, USA) and MATLAB (Mathworks, Natick, Massachusetts, USA). To correct motion artifacts and day-to-day positional variance, we employed a calibration program using image triangulation and piecewise affine transformation (TPAT), developed by our collaborators(*66*). All corrected images were also manually checked following a visual comparison method as quality control(*67*). Only data presenting consistent features including cells and blood vessels within the same field of view are deemed suitable for further analysis. Any data exhibiting significant uncorrectable vibration was classified as experimental failures and is therefore excluded from statistical analyses. Regions of interest (ROIs) representing neurons were manually labeled and the intensity of the cells was extracted in ImageJ. To best reduce signal interference from overlapping neurons on the same imaging plane, we've carefully adjusted the size of the ROI so that no overlapping regions occur. For example, for neurons that overlapped up to 50%, the size of all ROIs would be adjusted to less than the radius of cell bodies so that ROIs would not share signal sources. The intensity of all the pixels inside the cell body outline was averaged to calculate the raw calcium fluorescence intensity of the cell. For data presentation in Fig. 1H, a Gaussian smoothing filter was applied. Calcium transient traces were computed as the changes in relative fluorescence ($\Delta F/F_0$): $\Delta F = (F_i - F_0)/F_0$,

where F_i denotes the fluorescence intensity at any frame and F_0 denotes the basal fluorescence of each neuron. For each cell, the total calcium power for each imaging time point was calculated by taking the integrals of the raw calcium trace. To compare changes in neuronal ensemble activities after contextual fear conditioning training, we calculated the calcium dynamics in each ROI across various imaging time points (before training and delays respectively at 30 min, 28 d, 35 d, 39 d, 42 d, 46 d, 49 d, 52 d, 56 d, 59 d, 63 d).

Quantitative definition of "unsilenced cells"

To assess neuronal activation during the remote memory stage (day 28 to day 63, 4-9 weeks post encoding), we calculated normalized average calcium power for imaging time points at 28d, 39d, 42 d, 49 d, 52 d, 59 d and 63 d. Each imaging timepoint's average calcium power is calculated by taking the integrals of the raw calcium trace and then dividing it over the 90 s total time. Normalization is done by subtracting the before-training's average calcium power from each imaging timepoint's average calcium power. Before training average calcium power was thus calculated as zero. Neurons that maintained above zero normalized calcium power for every imaging time point from day 28 to day 63 (4-9 weeks, covering the remote memory stage) are defined as "unsilenced cells".

Corroboration of stable, training-specific feature of "unsilenced cells"

To determine whether the identification of "unsilenced cells" is influenced by arbitrariness in the selection of imaging time points, we performed random simulation experiments based on multiple remote-stage imaging time points. We randomly selected 1 up to 29 imaging time points during the remote stage from actual samples in one animal and calculated the average normalized calcium power. We then calculated the proportion of neurons with power values persistently above zero. We found that this proportion remains relatively unchanged when the total number of imaging time points considered exceeds 7 (reported in Fig. 1N). We thus selected 28 d, 39 d, 45 d, 49 d, 52 d, 59 d, 63 d, a total of 7 imaging time points one week apart to be considered in the identification process of "unsilenced cells".

To assess whether "unsilenced neurons" only existed in trained animals (CS-US group), we investigated temporal changes in average calcium power and spike frequency in CS-US and CS-only group (fig. S3D). Neurons with persistently elevated neuronal activities during every remote stage time points can only be observed in CS-US group, indicating that "unsilenced" neuron is training-specific. To statistically prove this observation, we also employed the bootstrapping method to compare CS-US group and CS-only group. Firstly, we constructed distribution of numbers of neurons fulfilling the quantitative definition of "unsilenced neurons" from randomized results (blue lines in fig. S3F). The randomized results were generated by shuffling the calcium power and spike frequencies of different neurons across all imaging timepoints, making the neuronal activities time independent. We then calculated the average probability value of finding an "unsilenced neuron" in 1000 randomly shuffled imaging results. This averaged probability was named as "true", though it must be noted that "true" do not refer to actual imaging observations. "True" represented the probability of neurons meeting "unsilenced" definition criteria after all data were rearranged in random scrambles. The bootstrapping results demonstrated that the "true" fell

right within the resampled distribution curve in CS-US group, but not in CS-only. These analyses collectively show that unsilenced neurons were unique to CS-US group.

Spike inference and synchronization calculation

To evaluate activation synchrony between neurons, calcium spikes representing neuronal action potentials (AP) were extracted. The time series of spike intensities for each neuron was thus converted into a binary sequence of 1 and 0 for each frame, with 1 denoting a spike and 0 denoting no spike. Since spike inference has inherent limitations and heavy dependence on the signal-to-noise ratio in the raw data, we utilized both DeepSpike inference(*32*) and a comparatively more conservative deconvolution method(*37*). Due to the different detection criteria in these two methods, DeepSpike has a higher inference accuracy in events (AP) occurrence while deconvolution at the most stringent threshold detects fewer false positive AP. Considering such features, we applied DeepSpike inference in the more dynamic-sensitive unsilenced neuron detection and information theory analyses. As synchronization analyses seek to identify highly synchronized cells and are prone to false positive bias, the deconvolution method was applied. We selected the highest threshold for deconvoluted spikes to maximumly reduced spike count and rule out false positives. In addition, we examined the performance of both methods by calculating false positive rates and accuracy values for all analyses. The false positive rate represents the proportion of negative signals that are incorrectly classified as positive. Accuracy represents the proportion of correctly classified spikes out of the total number of spikes. The low false positive rate (0.2 for DeepSpike and 0.1 for deconvolution) and high accuracy rate (0.8 for DeepSpike and 0.9 for deconvolution) validate the robustness of both methods.

With the spike-time information converted into binary series, each imaging frame yielded a multi-dimensional array consisting of 0 and 1. Based on inferred spike time series (binarized matrices consisting of 0 and 1, with 1 denoting one spike, and 0 denoting no spike, please see the diagram below), we counted the number of co-occurring spikes between a neuron (the target neuron) and any other neurons. For every imaging frame, if the target neuron was firing (“1”), we counted the spike number from all other neurons within that frame as the frame-wise synchronization count. If it didn’t fire (“0”), this frame is skipped. These frame-wise synchronization counts are added up across 2800 frames (90 s) to obtain synchronization counts for a single neuron.

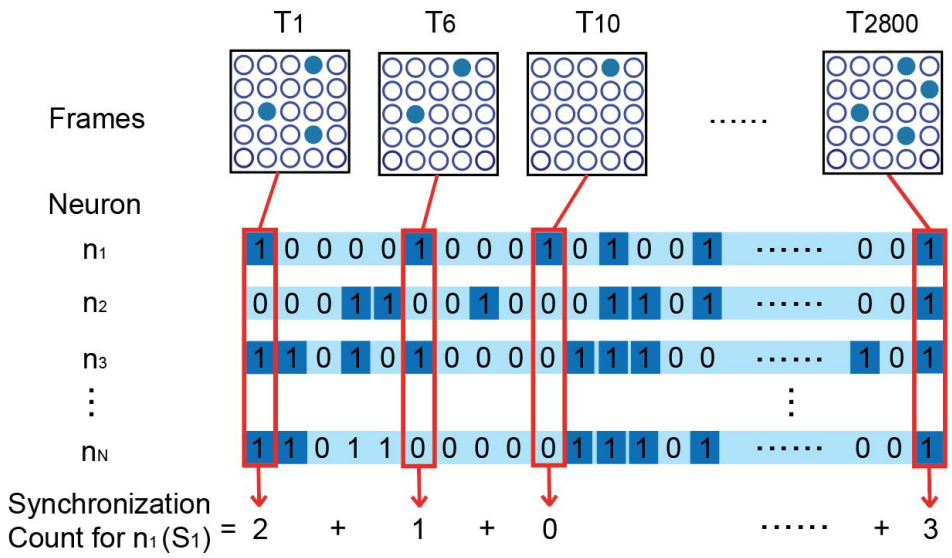

Next, the above process was repeated for all neurons in the imaging plane. Then the mean neuronal synchronization was taken as the total synchronization count S_{mean}:

$$S_{mean} = \frac{\sum_{i=0}^{N} S_i}{N-1}$$

Where N = the number of all neurons in the field of view.

Synchronization normalization for chance firing interference

Since high firing rates could cause chance elevations in synchronization counts, we corrected the raw counts by subtracting randomly shuffled results (the shift predictor). These procedures were proceeded by shuffling the original spike-time series in order to randomly assign the spikes to different frames (please see the diagram below). The shuffling procedure was repeated for 1000 times to generate the final averaged shift predictor which was then subtracted.

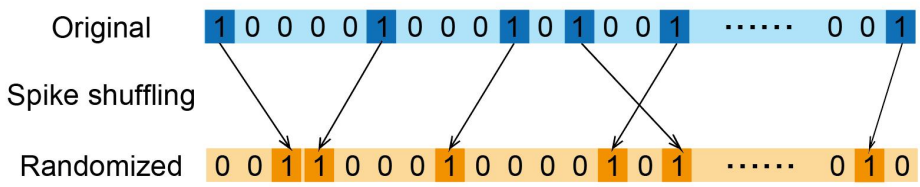

The corrected synchronization S_n

$$S_n = S_{mean} - S_r$$

Where S_r is the average synchronization count calculated based on randomized ensemble firing patterns. Randomization process illustrated above was carried out 1000 times for each neuron, and all resulting S_r values was averaged to obtain the final S_r value in equation. S_n for each imaging timepoint was calculated following steps above, and the result was reported in Fig. 3C.

Validation of synchronization normalization method

Since high-firing cells may cause chance elevation in synchronization counts, we tested the validity of our normalization method using the following procedures. To test the effect of high-firing rate upon synchronization, we conducted a simulation experiment (fig. S6). Utilizing MATLAB program, we generated two artificial neurons and measured the impact of their firing rates upon synchronization. We artificially set different synchronization counts for these two neurons to serve as the "ground truth". We then calculated normalized synchronization using between these two neurons using methods described above. We subtracted the "ground" truth from the calculated results to obtain error value of this method and assessed the effects of different sync. ratio on the error value (fig. S6B). The results showed that when the frequency of the neuronal activity (average firing rate) is less than 0.05, the original normalization method for synchronization impartially reflected the "ground truth" (fig. S6C). Since the average firing rate of actual neurons was close to 0.01 < 0.05, the original normalization method is applicable to our data.

To further corroborate that the synchronization analyses support our central claim, we also used another common normalization method of dividing the result by average neuronal firing rates. Specifically, for a neuronal ensemble that has N neurons, synchronization count of one neuron S at one imaging timepoints:

$$S = \frac{S_1}{(N-1)\sqrt[N]{r_1 \cdot r_2 \cdots r_N}}$$

Where S_1 denotes the raw synchronization count for neuron n_1 (please see diagram Fig), r denotes the firing rate of a single neuron. The firing rate is calculated as follows:

$$r = \frac{Total\ Spike\ Count}{number\ of\ frames}$$

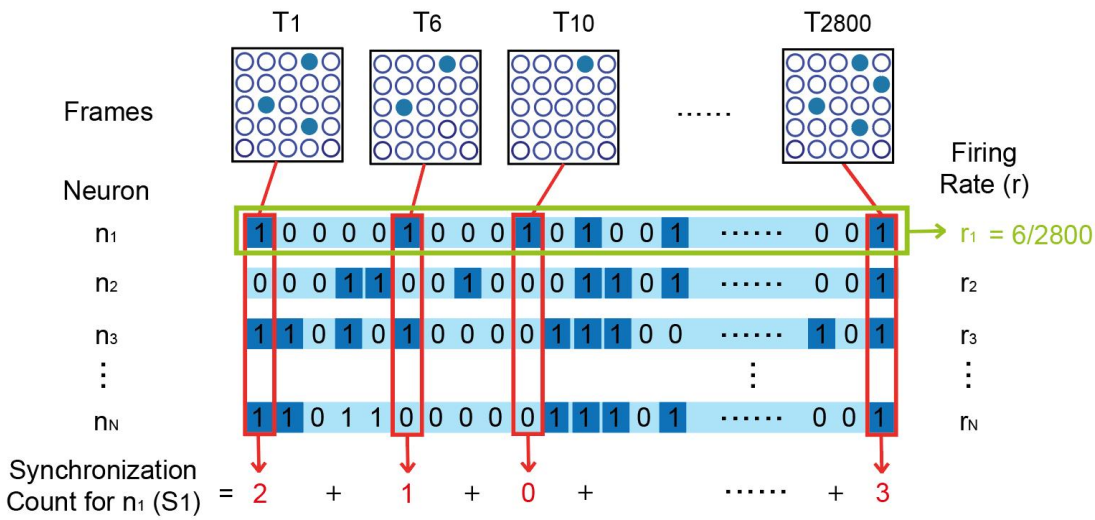

Then the sum of all neuronal synchronization was taken as the total synchronization count S_{mean}:

$$S_{mean} = \frac{\sum_{i=0}^{N} S_i}{N-1}$$

Where N = the number of all neurons in the field of view.

Lastly, corrected synchronization counts S_n was calculated as follows:

$$S_n = S_{mean} - S_r$$

Where S_r is the average synchronization count calculated based on randomized ensemble firing patterns. Randomization process illustrated above was carried out 1000 times for each neuron, and all resulting S_r values was averaged to obtain the final S_r value in equation.

This calculation method of normalized synchronization counts still supported our key observation in Figure 3. That is, neurons that maintain high synchronization counts throughout the remote stage (d28-d63) fully included all "unsilenced" neurons.

Definition of high sync. and low sync. neuron

Examination of synchronization counts for unsilenced neurons revealed that they maintained high synchronization (sync. counts ≥ 3σ) for every remote imaging timepoint from d28 to d63 (fig. S7A). Based on this phenomenon, we defined high sync. neurons as neurons that maintained sync. counts ≥ 3σ for every remote imaging timepoint (28d, 39d, 45d, 49d, 52d, 59d, 63d). Neurons with sync. counts < 3σ at any time point were defined as low sync. neurons.

We further tested this phenomenon in all GABAergic and non-GABAergic neurons using unsupervised clustering analysis. K-means clustering of standard deviation of Δ sync counts clearly showed that the high sync. neuronal group composed only of GABAergic neurons (fig. S7). Here Δ sync counts referred to the difference between the total sync. counts of each remote imaging timepoints (28d-63d) and the total sync. counts of before training baseline. Results from K-means clustering indicated that the existence of high and low sync groups is a phenomenon specific to GABAergic neurons (fig. S7).

Population vectors and ensemble similarity index calculation

Population vectors were calculated according to L. Carrillo-Reid et al.(*68*) Neural activity patterns at a single imaging frame (33 ms time bin) can be written as an n-dimensional vector, with n denoting the total number of neurons in the imaging plane. For each frame, the activities of all neurons were described as a vector and each cell was seen as a variable of the vector. One vector thus represents the ensemble response at one moment in time. Cosine similarity calculates the difference in the spatial angle of the multi-dimensional vectors and helps illustrate changes in ensemble patterns over time or under different stimulation conditions. The calculation formula is as follows:

For two multi-dimensional vectors A and B

$$cosine\ similarity = \frac{A \cdot B}{\|A\|\|B\|} = \frac{\sum_{i=1}^{n} A_i B_i}{\sqrt{\sum_{i=1}^{n} A_i^2}\sqrt{\sum_{i=1}^{n} B_i^2}}$$

Where A_i and B_i denotes the ith variable of vector A and B, respectively.

Complex network analysis

Weighted complex networks were used to describe the functional connections between the cells of the observed microcircuitry. Each cell was seen as a node of the complex network. We constructed the adjacency matrix of the complex networks from neural activity time series. Each element of the adjacency matrix (*W*) between a pair of cells denoted the count of how many times the two neurons fire simultaneously.

$$W = \begin{bmatrix} w_{11} & \cdots & w_{1n} \\ \vdots & \ddots & \vdots \\ w_{n1} & \cdots & w_{nn} \end{bmatrix}$$

Where adjacency matrix (*W*) was symmetric. The diagonal element was set as zero. We adopted two criteria to describe the properties of the microcircuitry. Firstly, the values in the weighted adjacency matrix denotes the functional connections between cell pairs. A bigger w_{mn} value indicates that the neuron pairs, *m* and *n*, are more tightly coupled in this observed microcircuitry. Secondly, the node strength (NS_p) denotes the total count of simultaneous spikes between a target cell *p* and all other cells in the observed microcircuitry. NS_p was calculated by

$$NS_p = \sum_{i=1}^{n} w_{pi}$$

Topology analysis

Topology analysis was based on the complex functional network analysis and was used to describe the structural dynamics of different functional neuronal ensembles. To build the coactivity complex of the key neurons, we applied the "sliding coactivity integration window" approach. This analysis converts neural coactivity into a simplicial complex, whose spatial structure is determined by the relative timing of spikes in a neural population. Firstly, we identify the maximal simplexes that emerge within the first time period, based on the cell activity rates evaluated, and construct the corresponding input integration coactivity complex. Then we calculated the functional network for the subgroup of cells in different experimental statuses.

Joint information entropy and joint mutual information analyses

Joint information entropy and joint mutual information analysis were conducted using the Neuroscience Information Theory Toolbox. (https://github.com/nmtimme/Neuroscience-Information-Theory-Toolbox). For each neuron, spike results were converted to a binary activation time series composed of 1 and 0, with 0 denoting no spikes, and 1 denoting a spike. These discrete-time series (lasting 90 s) of DeepSpike yielded calcium spikes at different imaging time points were used to calculate joint entropy and mutual information. Joint entropy between each neuronal pair is calculated by the following formula:

$$H(X,Y) = \sum_{x \in X,\, y \in Y} p(x,y) \log_2 \left(\frac{1}{p(x,y)} \right)$$

Where x denotes states (0 or 1, transcribed from DeepSpike inferred spike time series) of neuron X, and y denotes states of neuron Y. p (x = 1) denotes the calcium spike probability of neuron X, i.e., the ratio of the count of sampling points with calcium spike to the total sampling points. p (x = 0) = 1 – p (x = 1). p (x, y) denotes the joint probability distribution of neuron X and Y. p (x, y) has four states: p (x = 1, y = 1), p (x = 1, y = 0), p (x = 0, y = 1), p (x = 0, y = 0). The values of p (x, y) are determined by the spike time series of each neuron at each imaging time point. For example, p (x = 1, y = 1) denotes the ratio of the number of sampling points where both neurons X and Y have calcium spikes to the total number of sampling points.

Mutual information quantified the information that one neuron can provide about the second neuron and is calculated by:

$$I(X;Y) = \sum_{x \in X,\, y \in Y} p(x,y) \log_2 \left(\frac{p(x,y)}{p(x)p(x)} \right)$$

To test if the unsilenced neuronal ensemble demonstrates unique temporal dynamics in terms of information entropy, we compared their results to values generated from randomized controls. Randomized control samples were generated by shuffling the activation time series for each neuron. The spike order of each neuron was redistributed to randomly selected time points. The random experiments were repeated 10,000 times independently to get the average random measurements. To eliminate the influence of different neural activity strengths and improve the comparability of different experimental statuses, ratios between observed measurements and random measurements were calculated. To assess the training-induced changes in joint entropy and mutual information, we've also taken a second step of normalization, taking the ratio between measurements from each imaging timepoint and the measurements from before conditioning. Lastly, the population averages of normalized joint entropy and joint mutual information were calculated for various imaging time points.

Neural activity strength clustering analysis

Neural activity strength clustering analysis was used to find the key neuronal subgroup with high neural activities. Firstly, we calculated the spike count based on deconvolution and average amplitude of all calcium transients. Neural activity strength was associated with both the spike count and average amplitude. We set the baseline neural activity, denoting that the spike count and average amplitude were zero. We calculate each cell's neural activity strength compared to the baseline using Mahalanobis distance. The Mahlanobis distance is defined as:

$$\mathrm{D}(\mathrm{x},\mathrm{y}) = \sqrt{\max \sum_{\mathrm{i}=1}^{\mathrm{n}} \left[\mathrm{v}_{\varphi(\mathrm{i})}^{\mathrm{T}} \left(\mu_{\mathrm{x}} - \mu_{\mathrm{y}} \right) \right] / \lambda_{\varphi(\mathrm{i})}}$$

Whereas μ_x and μ_y are the average calcium signals from two neurons at each time session. $\lambda_{\varphi\ (i)}$ is the eigenvalues of the covariance matrix of the union of x and y. $V_{\varphi\ (i)}$ is the corresponding eigenvector and φ is a bijective mapping reordering indice of eigenvalues and eigenvectors. Second, we implemented hierarchical clustering for all cells based on their neural activity strength. The

inner squared distance (minimum variance algorithm) was used when constructing an agglomerative hierarchical cluster tree.

Community Analyses

The multi-layer complex functional network analyses were performed by the software Gephi9.3 (open-source). The built-in community analyses detect similarities among connectivity data based on node and edge values in a network. In our case node information is composed of the average normalized calcium power for each neuron; edge information is composed of the normalized pairwise synchronization counts (see synchronization calculation) between each node. Multi-layer networks are constructed for neuronal ensemble activities under different stimulation settings at retrieval to visualize and assess their differences. Gephi assigns a modularity class index to each constructed network. The calculation equation is as follows according to the Gephi manual:

$$Q = \sum_{c=1}^{k} \left[\frac{l_c}{m} - \left(\frac{d_c}{2m} \right) \right]$$

Where m is the total number of edges in the network; k is the number of communities; l_c is the number of connected edges within the community c; and d_c is the sum of the degrees of all the nodes in the community c.

Immunofluorescence

At the end of the 63-day experiment, histology of the imaged area was performed to assess neuronal health post long-term expression of rAAV2/9 viral tools. Mice were deeply anesthetized with tribromoethanol (0.02ml/g, intraperitoneally). Cardiac perfusion with 50 ml physiological saline and 25-50 ml 4% paraformaldehyde was performed sequentially. The brain was removed and immersed in 4% paraformaldehyde for 24 h at 4 °C. Then the brain was dehydrated in 40% sucrose for 3-6 days and frozen at -20 °C in optimal cutting temperature compound (OCT). Successive coronal sections of 30 μm were made with freezing microtome. The sections were mounted on slides with a mounting medium containing nucleic acid dye (DAPI, 4′,6-diamidino-2-phenylindole). Images were acquired using Nikon A1 confocal microscope with a 20 ×, 0.8 NA, and 40 ×, 0.6 NA objective lenses at 1024 × 1024 pixels. To count the number of GCaMP6f-positive cells and DAPI-positive nuclei, images of the ROI were acquired by ImageJ.

To examine the labeling efficiency and specificity of GABAergic neurons in GABA-Cre::Ai9 mice, we performed GAD67 immuno-staining. Coronal sections were prepared and mounted on slides following the above procedure. Then sections were first rinsed for 10 min × 3 times in PBS and blocked in PBS containing 10% donkey serum, and 3% Triton X at room temperature for 2 h. The primary antibody (#63080S, Cell Signaling Technology, In) was added and attached at 4 °C overnight. Then, sections were rinsed in PBS for 20 min and incubated with secondary antibodies (#A-31573, Thermo Fisher, Inc.) dissolved in PBS for 2 h at room temperature. Finally, sections were rinsed 3 times in PBS and mounted on slides with the nucleic acid staining mounting medium (DAPI, 4′,6-diamidino-2-phenylindole). For quantification, 7-10 z-stacks per animal were generated using a confocal microscope (Nikon, A1). Analysis by ImageJ revealed 100% signal co-localization with mCherry signals from report mice, consistent with the previous report.(*34*)

The neurotoxicity effect of long-term rAAV2/9 virus expression was assessed by TUNEL (terminal deoxynucleotidyl transferase-mediated dUTP nick-end labeling) Assay Kit (#64936, Cell Signaling Technology, Inc.). The toolkit enzymatically linked a fluorophore (640 nm) conjugated nucleotide to the 3' end of fragmented DNA. Sections were rinsed two times in PBS for 5 min each, permeabilized in PBS-TB for 30 min, and then washed again two times in PBS for 5 min each. Then sections were incubated in 100 μL TUNEL Equilibration Buffer for 5 min. 50 μL of TUNEL reaction mix (1 μL of TdT Enzyme added to 50 μL of TUNEL Reaction Buffer) was added to each slide. Then sections were incubated for 60 min at 37°C protected from light. Post incubation, sections were rinsed three times in PBS-TB for 5 min each. The slides were finally covered with a mounting medium containing nucleic acid dye (DAPI, 4′,6-diamidino-2-phenylindole). 7-12 z-stacks per animal were acquired using a confocal microscope (Nikon, A1). Co-localization of GCaMP6f, C1V1(T/T), eNpHR3.0 and TUNEL fluorescence was examined in ImageJ (fig. S1). Analysis revealed a 1.29% apoptosis rate in GCaMP6f+ cells. Among all GCaMP6f+ cells, 11.93% of TUNEL+ cells were found at the injection injury site (30-50 μm radius), 1.08% near injury (50-130 μm radius), and 0.07% away from injury. To test whether apoptosis was caused by physical injury of the glass syringe, we inserted needle without the virus and counted TUNEL+ neurons (fig. S1C). We found that the majority of TUNEL+ cells resided at the injury site, suggesting that physical injury was the main cause of apoptosis. No significant neurotoxicity effect was found for long-term rAAV2/9 viral tools expression.

In vivo whole-cell electrophysiology

In vivo whole-cell electrophysiology was performed under two-photon imaging. Borosilicate glass pipettes (6–8 MΩ) were pulled by horizontal micropipettes puller (P-97, Sutter Instrument, USA) and filled with an intracellular solution (135 mM potassium methylsulfate, 8 mM NaCl, 10 mM HEPES, 2 mM Mg-ATP, 7 mM phosphocreatine, 0.01 mM d-Bicuculline, 0.02 mM Alexa Fluor 594, with 7.3 pH, 316 mOsm). Pipettes were positioned using a micromanipulator (MP-225, Sutter Instrument, USA). Data was recorded with a Axopatch-700B amplifier (Molecular Devices, Palo Alto, CA) and was low-pass filtered at 2 kHz and acquired at 5-10 kHz. Collected data was processed with the pClamp10.1 software and analyzed using Clampfit 10.1 (Molecular Devices, Palo Alto, CA).

Statistical analysis

All statistical analyses were performed using GraphPad Prism software (GraphPad Software, Inc., La Jolla, California, USA). The data were presented as the mean ± SEM (Standard error of mean). Parametric analyses were performed using one-way ANOVA with Tukey post-hoc tests. Nonparametric analyses were performed using Friedman test with Dunn's correction for multiple comparisons. Statistical significance threshold was set at 0.05, and significance levels were presented as $*P < 0.05$, $**P < 0.01$ in all figures unless otherwise noted.

Supplementary Figures

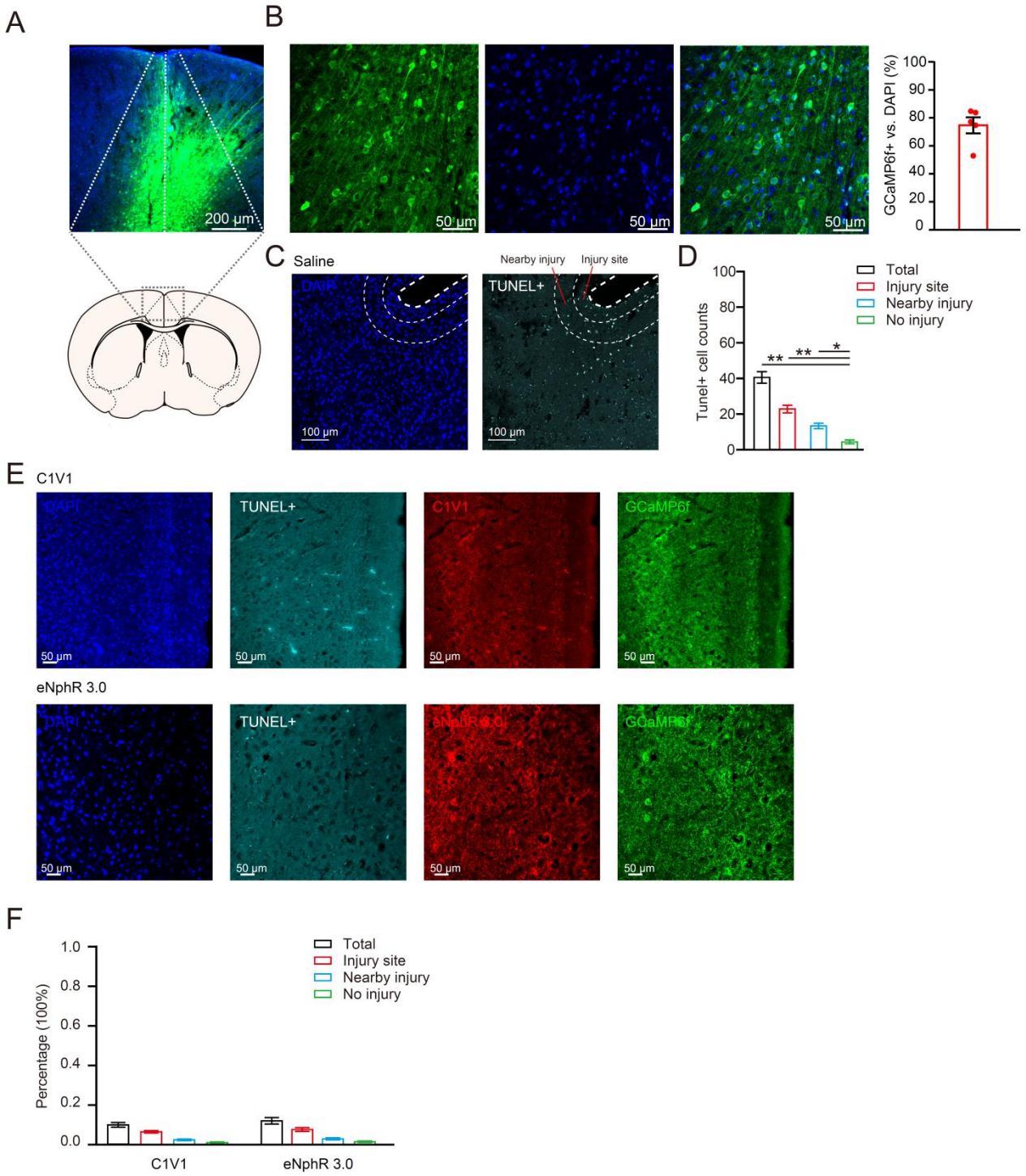

Figure S1. Verification of injection, viral expression and neuronal health post long-term expression of rAAV2/9. (A) Location of rAAV2/9-hsyn-GCaMP6f injection and expression in right anterior cingulate cortex (rACC, AP: 0.26 mm, ML: -0.35 mm, DV: 0.30 mm). **(B)** Histology of GCaMP6f positive cells (green) and all ACC neurons (blue, DAPI stained). Numbers of cells were manually counted and percentage of GCaMP6f + cells versus DAPI stained cells was 73.51 ± 5.67 (Mean ± SE). Scale bar: 50 µm. **(C)** Apoptosis near injection location assessed by TUNEL assay (n=7 slices from 2 animals). The injury site was defined by 30-50 µm radius around the needle

lesions; “nearby injury” was defined by 50-130 μm radius. **(D)** Total number of TUNEL+ cells in 12 slices from 3 animals. Total = 40.58 ± 3.18 number of cells, injury site = 22.83 ± 2.14, nearby injury = 13.33 ± 1.53, no injury = 4.42 ± 1.16. Total vs. No injury, $P < 0.0001$, injury site vs. No injury, $P < 0.0001$, nearby injury vs. No injury, $P = 0.03 < 0.05$, one-way ANOVA. **(E)** Location of rAAV2/9-hsyn-C1V1, rAAV2/9-hsyn-eNpHR3.0 and GCaMP6f injection, expression and TUNEL assay signals in right anterior cingulate cortex. **(F)** Percentage of number of TUNEL+ cells in 12 slices from 3 animals of each group. The injury site was defined by 30-50 μm radius around the needle lesions; “nearby injury” was defined by 50-130 μm radius; “no injury” was defined by the rest of the imaged areas. C1V1: Total = 10.01 % ± 1.16 %, injury site = 6.50 % ± 0.62 %, nearby injury = 2.46 % ± 0.42 %, no injury = 1.06 % ± 0.38 %. eNphR3.0: Total = 12.10 % ± 1.62 %, injury site = 7.66 % ± 0.93 %, nearby injury = 2.92 % ± 0.53 %, no injury = 1.53 % ± 0.38 %.

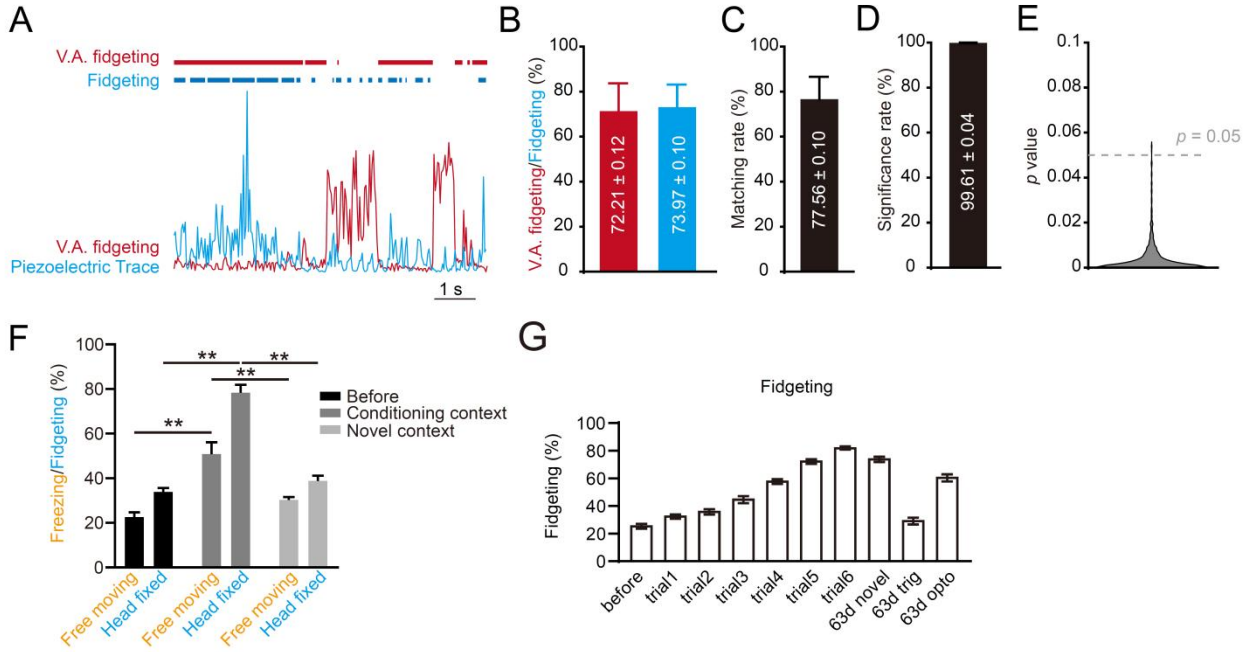

Figure S2. Behavioral specificity of piezoelectric signals. (A) Correspondence between fidgeting behaviors, assessed by video analyzation (V.A.) and piezoelectric sensor signals respectively. Top, short lines indicate periods of identified V.A. fidgeting and fidgeting behavior. Bottom: raw piezoelectric signals (blue) and raw V.A. fidgeting index (red) during last trial of training. V.A. fidgeting index indicate the gripping actions (assessed by frame-to-frame difference) of animals' front paw. When the animals were shocked, they became motionless and tightened their front paw grip. The motionless period was picked by frame-to-frame comparison algorithm in video analysis (calculated as V.A. fidgeting value). Small V.A. fidgeting value reflects no motion. The tightened front paw grip accompanied no motion response and was reflected by increased foot pressure captured by the piezoelectric sensor. Therefore, small V.A. fidgeting values correspond to large piezoelectric signals, which respectively reflect the fidgeting response. **(B)** Comparable percentage of fidgeting and V.A. fidgeting response from sample shown in A. **(C)** Matching rate between labeled fidgeting and V.A. fidgeting response from the sample in A. **(D)** Significance rate ($P < 0.05$) of 1000 t-tests based on simulated fidgeting score of remote memory retrieval and before conditioning. 99.61% significance rate indicated that 99.61% of p-values were smaller than 0.05 in all simulations. **(E)** Remote memory retrieval induced significantly higher fidgeting compared to before even for simulated p-values (overall distribution < 0.05). **(F)** Side by side comparison of fear conditioning results measured by percentage of freezing (free moving) and fidgeting (head fixed) respectively. Free moving CFC: before = 22.50 % ± 2.22 %, old = 50.75 % ± 5.39 %, novel = 30.25 % ± 1.32 %, old vs. before, $P = 0.0007 < 0.001$, novel vs. before, $P = 0.299 > 0.05$, old vs. novel, $P = 0.006 < 0.01$; Head fixed CFC fidgeting%: before = 33.75 % ± 1.89 %, old = 78.25 % ± 3.64 %, novel = 38.75 % ± 2.39 %, old vs. before, $P < 0.0001$, novel vs. before, $P = 0.435 > 0.05$, old vs. novel, $P < 0.0001$, n=4 animals. **(G)** Conditioning trial-averaged fidgeting response demonstrated successful formation of associative memory. Before: 25.33 ± 1.76, trial 1: 32.25 ± 1.53, trial 2: 35.75 ± 1.88, trial 3: 44.58 ± 2.57, trial 4: 57.58 ± 1.77, trial 5: 72.08 ± 1.68, trial 6: 82.00 ± 1.16, 63d trig: 73.67 ± 1.90, 63d novel: 29.08 ± 2.52, 63d opto: 60.25 ± 2.61; trial 1 v.s. Before: $P = 0.30 > 0.05$, trial 2 v.s. Before: $P = 0.0121 < 0.05$, trial 3 v.s. Before: $P < 0.01$, trial 4

v.s. Before: $P < 0.01$, trial 5 v.s. Before: $P < 0.01$, trial 6 v.s. Before: $P < 0.01$, 63d trig. v.s. Before: $P < 0.01$, n = 12 animals, one-way ANOVA, mean ± s.e.m.

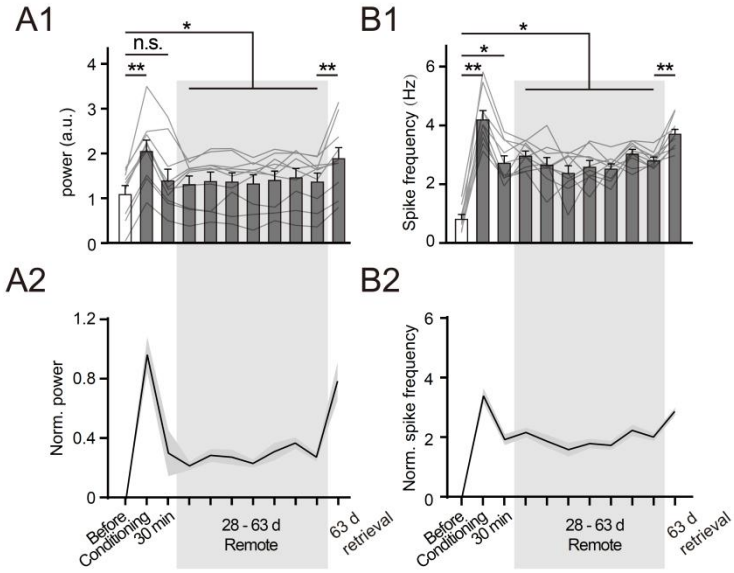

Figure S3. Unsilenced neurons remain in an intermediate activity level until being further activated upon retrieval. Comparing retrieval and default activities revealed the convergent dynamic feature of these neurons across subjects. Activities of unsilenced neurons during retrieval (shown in red box) were much higher than default potentiated activities during the remote stage, indicating that these cells remain in an intermediate state until being further activated by retrieval cues. A1&B1, original values of calcium power and spike frequency. A2&B2, normalized calcium power and spike frequency showing the difference between post-training and before training activities.

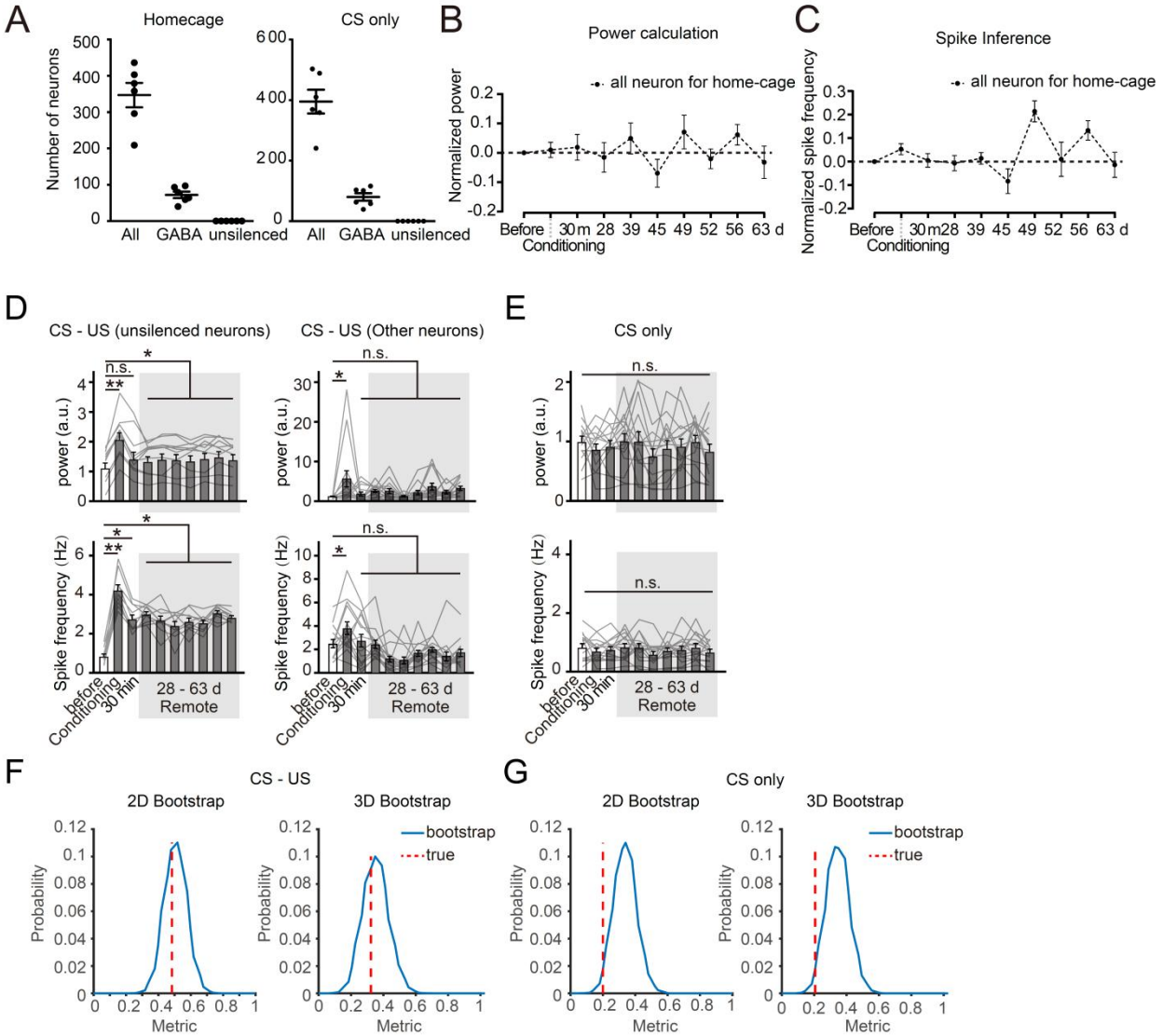

Figure S4. Absence of unsilenced neurons in CS only group. (A) Distribution of neuronal types in control groups. No unsilenced neurons identified for CS-only and home caged groups. Home-caging: All neurons: 346.83 ± 33.59, GABA neurons: 72.00 ± 8.89, unsilenced neurons: 0.00 ± 0.00, CS only: All neurons: 395.17 ± 39.33, GABA neurons: 80.54 ± 12.54, unsilenced neurons: 0.00 ± 0.00, mean ± s.e.m. **(B)** Normalized calcium power dynamics in all neurons in home caged groups. Stochastic changes around before-conditioning baseline were observed at remote stage. **(C)** Normalized calcium spike counts in all neurons in home caged groups confirmed results of power calculation. Spikes were inferred using DeepSpike method. **(D)** Unsilenced neurons in CS-US group showed more elevated average power and spike frequency during remote stage compared to other neurons. Gray lines, results from individual neurons. Gray area, remote memory stage. Unsilenced neurons, before vs. cond. $P < 0.001$; before vs. remote, $P < 0.05$; L1, before vs. cond. $P < 0.01$, before vs. 30 min, $P < 0.05$, before vs. remote, $P < 0.01$; Other neurons, before vs. cond. $P < 0.05$, each timepoint's value was compared to before's value using nonparametric Friedman test with Dunn's correction for multiple comparisons, n = 52 neurons for unsilenced and other randomly selected neurons respectively from 12 animals). **(E)** No distinct pattern in average power and spike

frequency can be identified for CS-only neurons. Power: P = 0.999 > 0.05, spike frequency: P = 0.999 > 0.05, n=78 neurons in 5 animals, one-way ANOVA, Dunn's multiple comparisons test. **(F)** Bootstrap analysis for 2D and 3D imaging in CS-US group. Overlap of estimator (red) and distribution (blue) in CS-US group indicate the presence of unsilenced neurons. n = 5 animals. Blue lines, the bootstrapped curve of neuronal spikes at all time points. Red dotted line, the average probability value of finding an "unsilenced neuron" in 1000 randomly shuffled imaging results. **(G)** Bootstrap analysis for 2D and 3D imaging in CS-only group. Separation of estimator (red) and distribution (blue) in CS-only group suggest that unsilenced cells were absent.

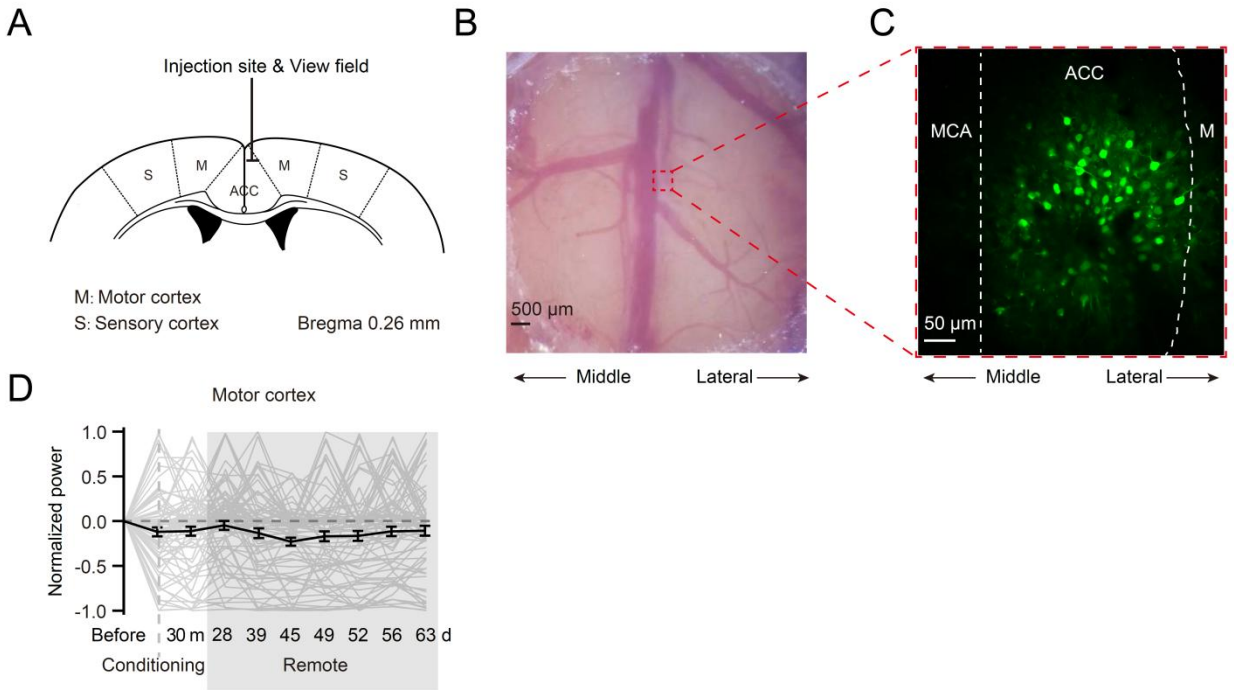

Figure S5. Corroboration of ACC targeting and region-specificity of unsilenced neurons. (A) FOV location on the mouse brain atlas, coronal section at 0.26 mm anterior to the bregma. **(B)** Photo of the cranial window. Location of the FOV marked by red dotted lines. **(C)** Sample FOV (averaged across 2800 frames). Location of the middle cerebral artery (MCA), ACC, and the motor cortex (M) were marked by white dotted lines. **(D)** Absence of unsilenced neurons in the neighboring motor cortex. No neurons in neighboring motor cortex maintained persistent above-zero average calcium power at remote time points (28-63d), indicating that unsilenced neurons could not be identified in the motor cortex. Black lines, average calcium power. Gray lines, individual neuronal calcium power. Remote stage results were shaded in gray.

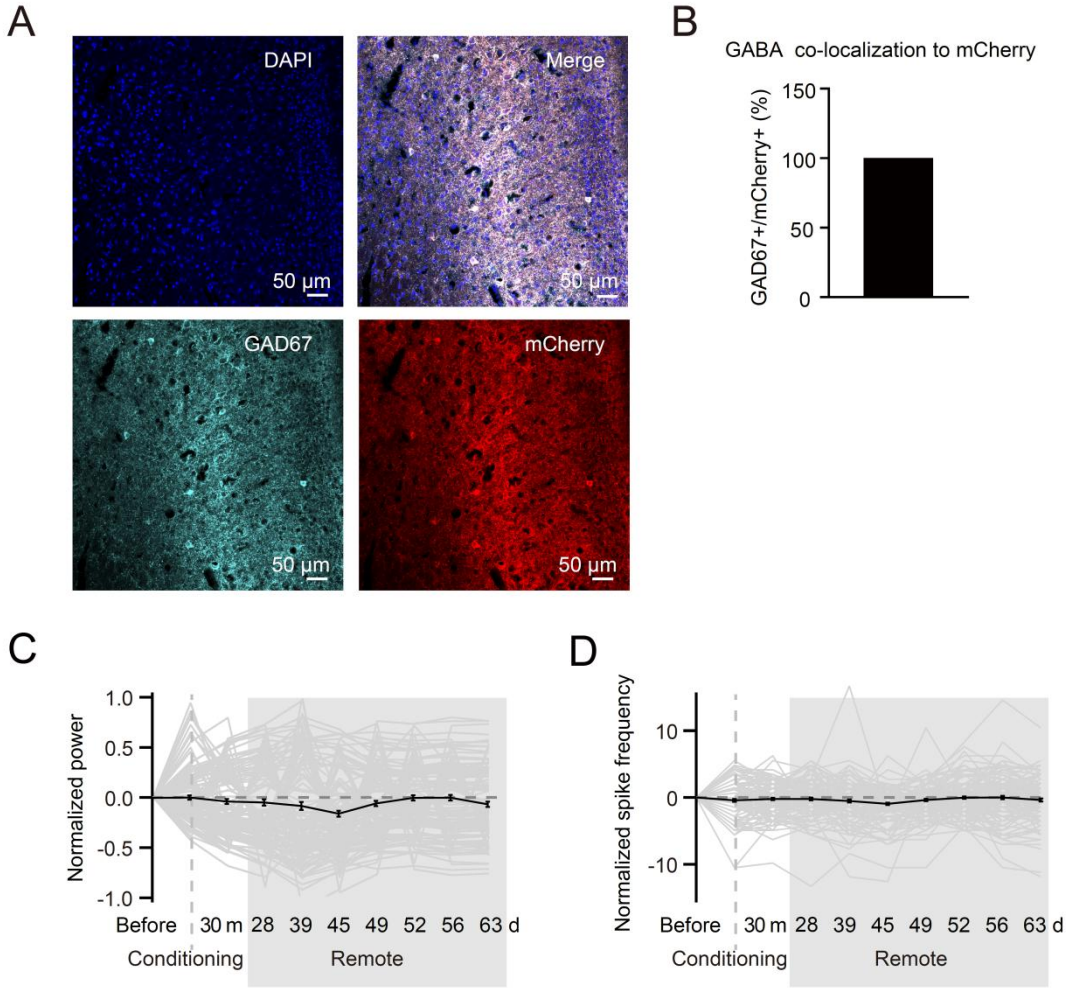

Figure S6. GABAergic labeling efficiency in GABA::Ai9 mice. (A) Histology evaluating report specificity and accuracy of GABA :: Ai9 mice reporters. **(B)** GAD67+ cells and mCherry signals show 100% co-localization in the ACC region. GAD67+ cells / mCherry+ cells = 100%, n = 6 ROIs from 6 slices of 2 animals. **(C)** Activities of all GABAergic neurons fluctuate around baseline during remote memory stage, as opposed to unsilenced neurons. Values at each imaging timepoints were normalized by subtracting the before conditioning baseline value. Black lines, average normalized power. Gray lines, individual neuron normalized power. Gray area, remote memory stage. n = 113 neurons from 1 sample animal. **(D)** Normalized spike frequency of all GABAergic neurons.

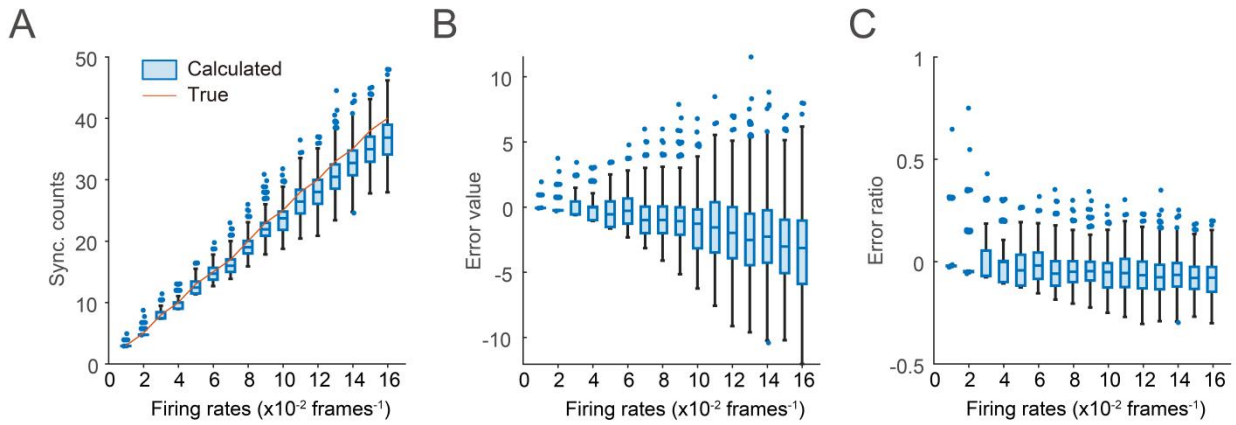

Figure S7. Assessment of synchronization normalization method by simulation experiment. (A) Sync. counts value calculated and normalized with original methods was comparable to ground truth sync. counts at all firing rate levels. Firing rate was obtained from firing counts of two artificial neurons within one imaging frame. **(B)** Smallest error value was obtained at firing rates smaller than 0.01. Error value was calculated by taking the difference between calculated sync. counts and ground truth sync. counts. **(C)** The smaller the firing rate, the smaller the error ratio in the 1000 simulations. For firing rate smaller than a certain level (e.g. 0.01), error ratio in synchronization estimation was neglectable. Error ratio was calculated by dividing the error value with calculated sync. counts.

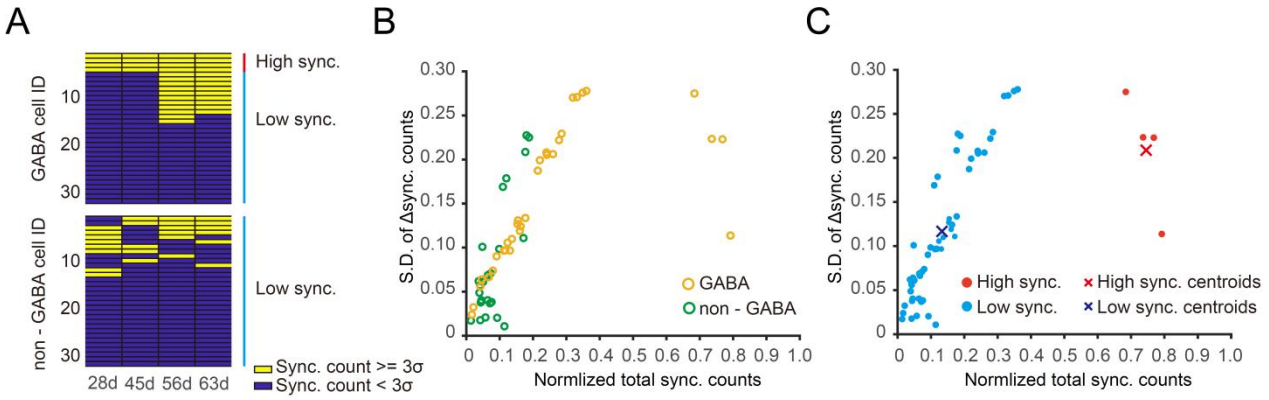

Figure S8. Two neuronal groups with distinct synchronization stability were identified in GABAergic neurons, but not in non-GABAergic neurons. (A) No high sync. neurons (red bar) could be identified in non-GABAergic cell groups. Yellow indicated that the neuronal sync. count ≥ 3σ at a specific timepoint. For a cell to be identified as "high sync.", all four remote timepoints (28d-63d) needs to be yellow. Blue indicated low sync. neurons (sync. count < 3σ). **(B)** Distinction between GABAergic and non-GABAergic neurons in distribution of Δ sync. counts' standard deviation and normalized total sync. counts. **(C)** Unique cluster of high sync. neurons existed only in GABAergic neurons, but not non-GABAergic neurons. K-means values were calculated by the Euclidean distance.

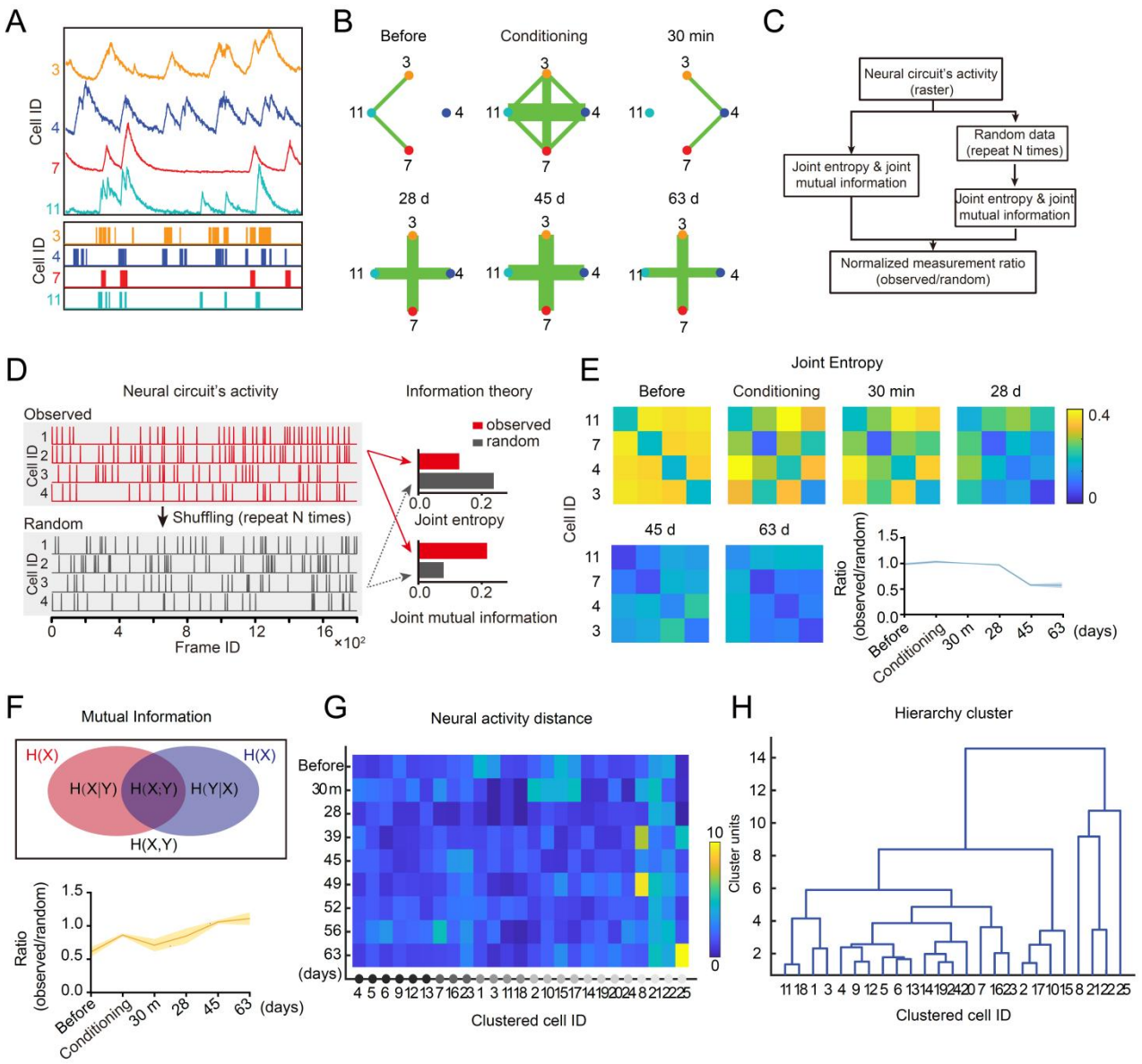

Figure S9. Unsilenced neurons constitute a stable topological network for efficient information processing. (A) Calcium spikes inferred from raw calcium transients using DeepSpike. Colored numbers indicate unsilenced neuron IDs. **(B)** Topological map of unsilenced neuronal ensembles at different stages of contextual memory formation. Topology reflects how synchronized firings are processed by the readout neurons. Node colors indicate cell IDs in panel A. Line thickness indicates the stabilization probability of the functional connectivity between each node (for calculation methods, see supplementary materials). **(C)** Flow chart of joint information entropy and mutual information analyses. **(D)** Observed unsilenced ensemble activities show higher capacity for information processing compared to that of the randomized control. Left, a randomized control was generated by shuffling neuronal spike time series N times. Right, diagram of parameters calculated from real data (observed) and randomly generated samples (random). **(E)** Decreased joint information entropy in unsilenced neurons supports efficient information processing at remote stages. Top and bottom left, joint information entropy of unsilenced neurons (n = 4 neurons, 1 animal). Heatmaps mirrored along the diagonal line. Bottom right, temporal changes show decreases in averaged normalized joint entropy at the remote stage (Before: 0.987 ± 0.021,

Conditioning: 1.032 ± 0.024, 30 min: 1.002 ± 0.001, 28 d: 0.970 ± 0.018, 45 d: 0.576 ± 0.020, 63 d: 0.571 ± 0.053, n = 5 animals, mean ± s.e.m.). Low information entropy values at remote time points indicate high nonlinear correlations in pairwise neuronal activities. Normalization is performed by taking the ratio between the observed sample results and random sample results. **(F)** Increased joint mutual information of unsilenced neurons at the remote stage supports efficient information processing. Top, diagram showing the calculation method for mutual information. Bottom, temporal changes in average normalized joint mutual information (Before: 0.611 ± 0.074, Conditioning: 0.867 ± 0.022, 30 min: 0.714 ± 0.094, 28 d: 0.852 ± 0.114, 45 d: 1.064 ± 0.029, 63 d: 1.114 ± 0.094, n = 5 animals, mean ± s.e.m.). **(G)** Mahalanobis distance between ensemble activities at each imaging time point and activities before training. The results are from all observed GABAergic neurons. The color bar indicates the distance value. Cells that possess large distances underwent drastic activity shifts during remote stages compared to before conditioning (unsilenced neurons 8, 21, 22, 25). n = 24 neurons in 1 animal. **(H)** Hierarchical clustering analysis indicates that unsilenced neurons (8, 21, 22, 25) are clustered and display similar activity patterns. Clustering was based on Mahalanobis distances further revealed the shortest within-group distance among unsilenced neurons, indicating their convergence in temporal activity dynamics.

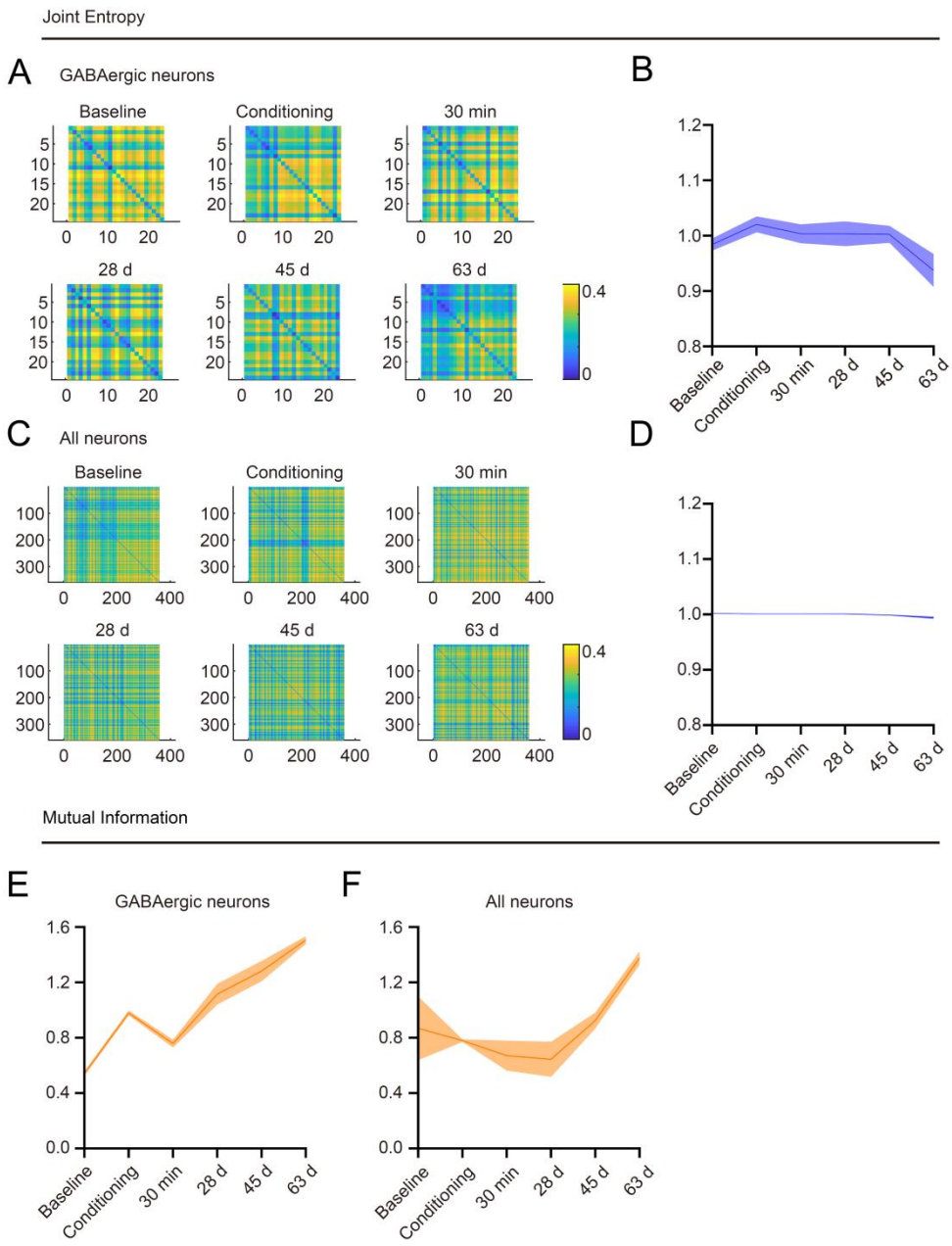

Figure S10. Joint information entropy and mutual information dynamics of all GABAergic neurons and the entire imaged population. (A) Joint information entropy for all GABAergic neurons imaged across different time points in 1 animal. Vertical axis denotes cellular ID number. **(B)** Temporal changes in average normalized joint information entropy for all GABAergic neurons. Mean ± s.e.m. Normalization was performed by taking ratios between observed and randomly shuffled control samples' results. Similar to results for unsilenced neuronal ensembles, normalized joint information entropy showed a decreasing trend at the remote stage. **(C)** Joint entropy for all neurons (GABAergic and non-GABAergic neurons) imaged across different time points in 1 animal. **(D)** Temporal changes in normalized joint information entropy for all neurons. The small variance in entropy derived for collective neuronal activities indicate strong stochasticity in their activation patterns. **(E)** Temporal changes in normalized mutual information for GABAergic neurons. Mean ± s.e.m. **(F)** Temporal changes in normalized mutual information for all neurons. Mean ± s.e.m.

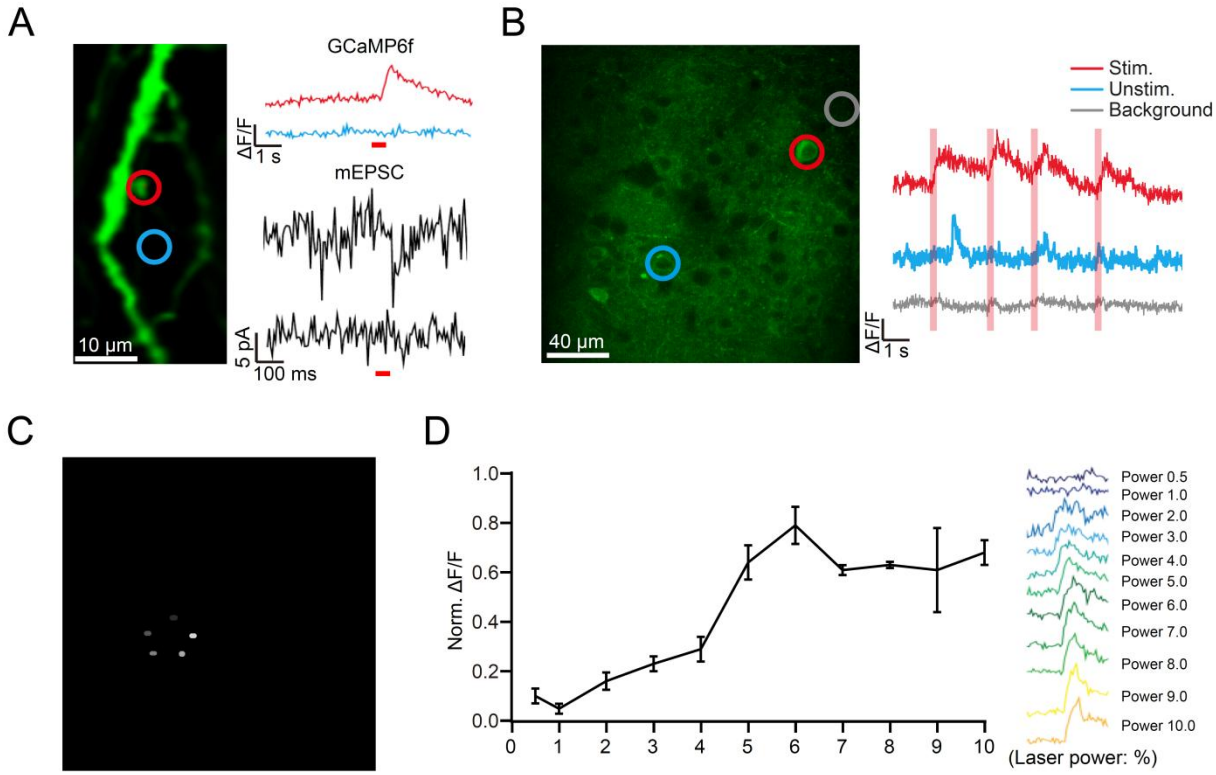

Figure S11. Precision verification of two-photon holographic optogenetic stimulation. (A) Holographic stimulation by galvano-galvano lens of a single spine (red) created mEPSPs while a proximal stimulation (blue) did not. Left, selected stimulation ROIs. Top right, calcium transients (ΔF/F) for the bouton (red) and control position (blue) respectively post stimulation. Bottom right, mEPSP recorded at the soma via *in vivo* patch-clamp. Red bar indicates light stimulation. **(B)** Effect of stimulation in an example imaging field. Left, stimulation ROIs where stimulated neuron was circled in red, unstimulated neuron in blue and control ROI containing no neurons circled in grey. Right, GCaMP6f fluorescence transient (ΔF/F) trace for respective ROIs in B. Bar indicate stimulations. **(C)** Simultaneous stimulation of 5 ROIs on a fluorescence plate using the SLM method. **(D)** Line chart of averaged calcium signal showing increase for stimulation at different power levels. Right, ΔF/F trace for each power level.

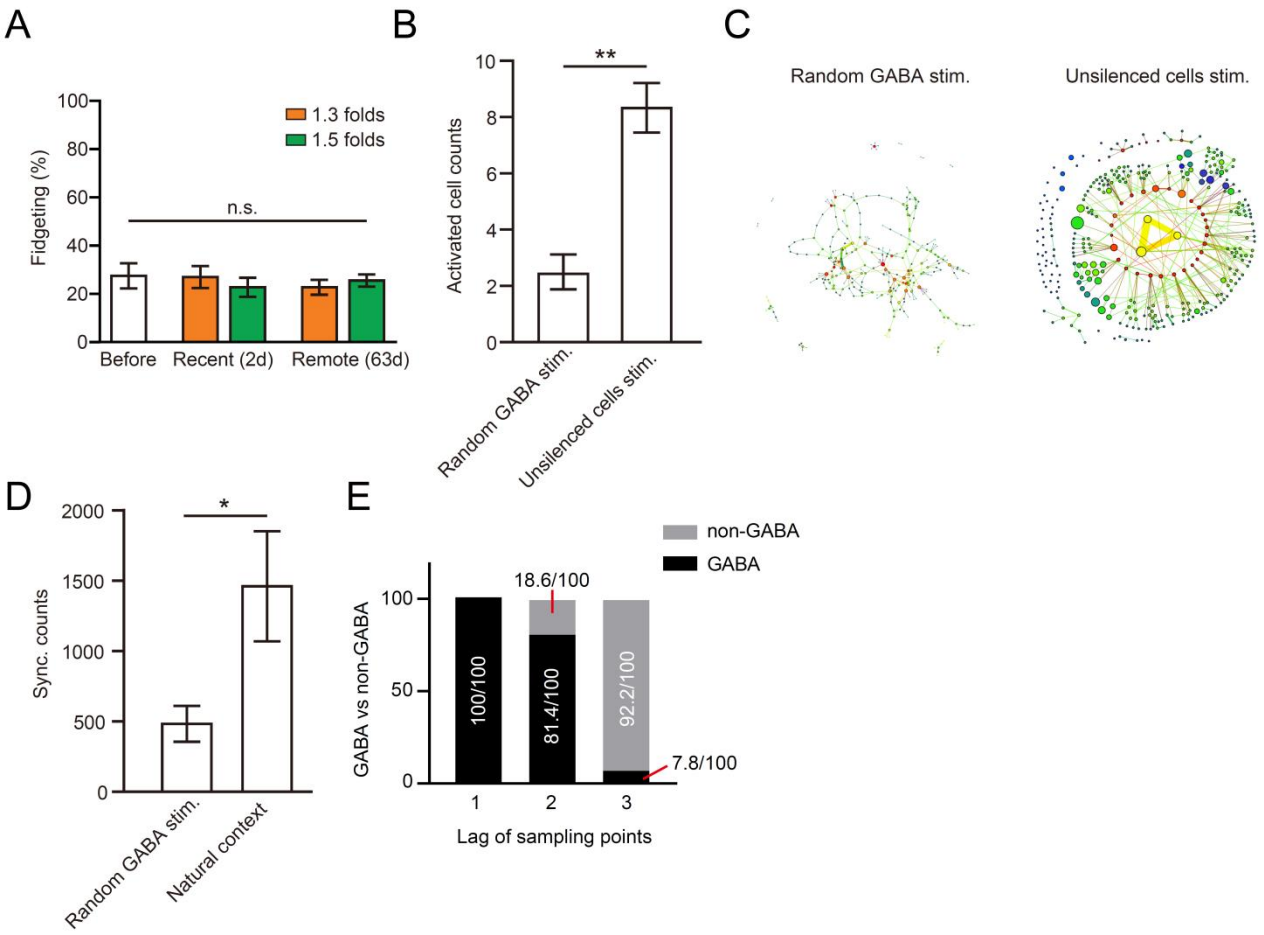

Figure S12. Random GABAergic cell stimulation failed to retrieve remote memory and memory-related hierarchical ensembles. (A) Random activation of memory-related GABAergic cells failed to retrieve remote memory. Memory-related GABAergic cells were defined by neurons with increased activities during encoding compared to before training baseline. 1.3 folds and 1.5 folds referred to neurons with respective 30% and 50% activity increment during conditioning stage compared to before training baseline. 1.3 folds: before = 27.25 ± 5.17, recent = 27.00 ± 4.55, remote = 22.75 ± 3.97, recent vs. before, P = 0.94 > 0.05, remote vs. before, P = 0.74 > 0.05. 1.5 folds: recent = 22.75 ± 3.07, remote = 25.50 ± 2.50, recent vs. before, P = 0.99> 0.05; remote vs. before, P = 0.96 > 0.05, n=4 animals, one-way ANOVA. **(B)** Fewer neurons fired in the first frame (33ms) after holographic stimulation of random GABAergic neurons compared to unsilenced neurons. Unsilenced cells stim. = 8.33 ± 0.88, random GABA stim. = 2.50 ± 0.62, P = 0.0003 < 0.001, n = 6 animals, two-tailed t test. **(C)** Sparser evoked downstream pattern by random GABAergic neurons stimulation compared to unsilenced neurons. **(D)** Weaker functional connection between downstream neurons under random GABAergic stimulation compared to natural context recall. Random GABA stim. = 482.72 ± 127.37, natural context = 1461.02 ± 391.16, P = 0.0387 < 0.05, n = 6 animals, two-tailed t-test. Functional connection was measured by count of synchronization events (sync. counts) between neurons within the first frame (33ms) after opto. stimulation. **(E)** GABAergic neurons demonstrated closer follow-up activation to unsilenced neurons compared to non-GABAergic neurons. Y-axis, number of GABAergic vs. non-GABAergic neurons within 3 frames after optogenetic stimulation of unsilenced neurons. Lag of sampling

points indicate the order of frames following unsilenced neuron activation. Lag1 = 100 vs. 0; lag2 = 81.40 vs. 18.60; lag3 = 7.80 vs. 92.2, n=5 animals.

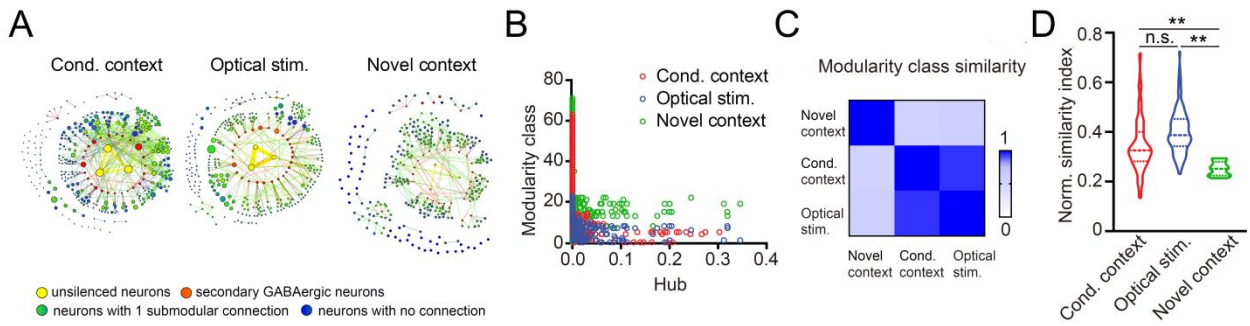

Figure S13. Unsilenced neuron activation elicited a disinhibitory hierarchical network relevant for successful retrieval. (A) Community analysis of neuronal ensembles evoked under various conditions. Optogenetic and contextual stimuli elicit similar multilayer modules, while novel contexts elicit drastically different interneuronal connection strengths and submodular structures. Color gradients and networks illustrate modular patterns between neurons. Node sizes positively correlate to averaged calcium transients of each neuron. **(B)** Modularity class distribution of neuronal ensembles activated under different treatments. Modularity classes were calculated from C and denoted community separation. Greater distribution overlap exists between the ensembles elicited by cond. context (red dots) and optogenetic stim. (blue dots) compared to the novel context (green dots). **(C)** Modularity class similarity calculation confirmed the highest community similarity under opto. stimulation. and cond. context treatments. The similarity index is calculated by Pearson's correlation coefficient between distributions of modularity class numbers under respective conditions. n = 330 neurons in 1 animal. **(D)** Population distribution of normalized modularity class similarity. Normalization is performed by taking the ratio between each modularity class number and the mean. Cond. Context vs. Opto. stim., $P = 0.25 > 0.05$, Cond. Context vs. Novel context: $P = 0.0004 < 0.01$, Opto. stim. v.s. Novel context, $P < 0.01$, n = 400 neurons from 4 animals.

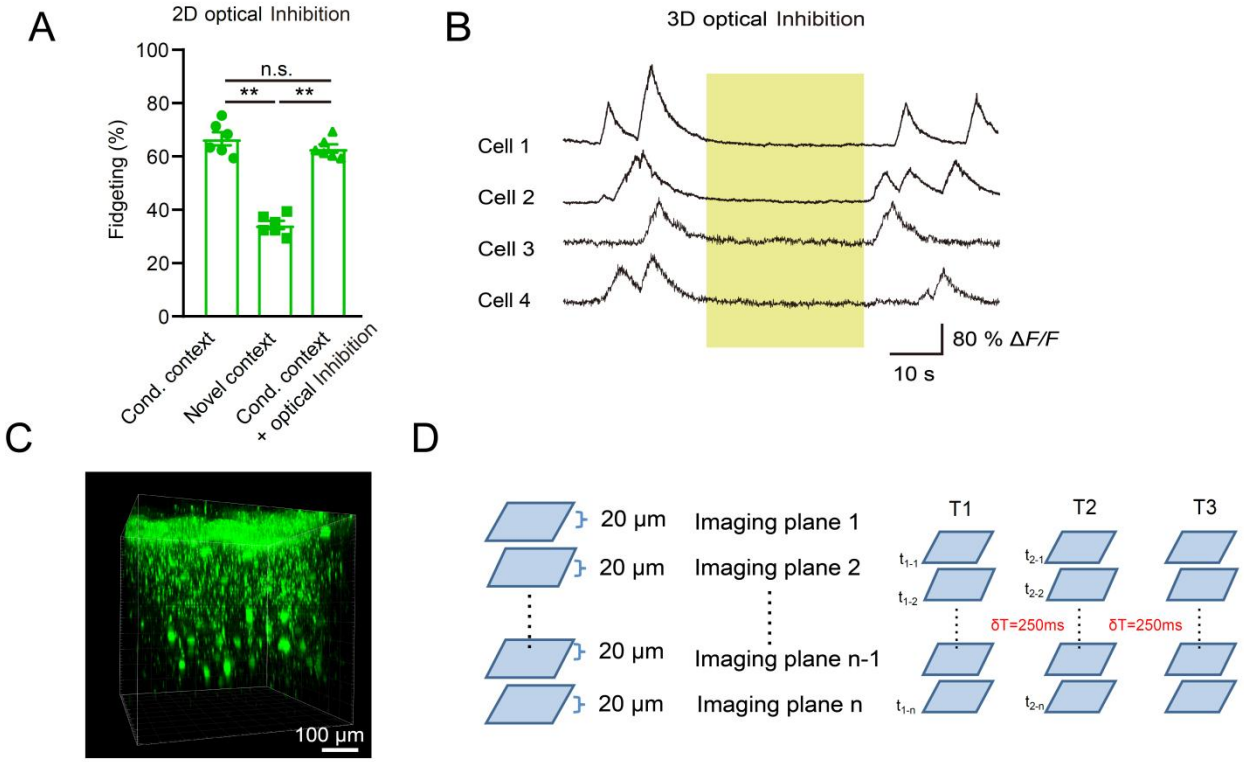

Figure S14. Observations on 2D and 3D optogenetic inhibition of unsilenced neurons. (A) Holographic inhibition of unsilenced neurons in the imaging plane during memory retrieval test failed to significantly reduce fidgeting response. Cond. context: 66.33 ± 2.47 %, Novel context: 34.00 ± 1.51 %, Opto. Stim.: 62.67 ± 1.52 %; Cond. context v.s. Novel context: $P < 0.01$, Cond. context v.s. Opto. Stim.: $P = 0.38 > 0.05$, Opto. Stim. v.s. Novel context: $P < 0.01$, n = 6 animals, one-way ANOVA, mean ± s.e.m. **(B)** GCaMP6f fluorescence transient (ΔF/F) trace evoked by holographic inhibition shows sustained inhibitions in randomly selected test neurons. Bar indicate inhibitory stimulations. **(C, D)** Diagram of sampling process for 3D volumetric imaging and inhibition. Total collection time was 250 ms for each volume.

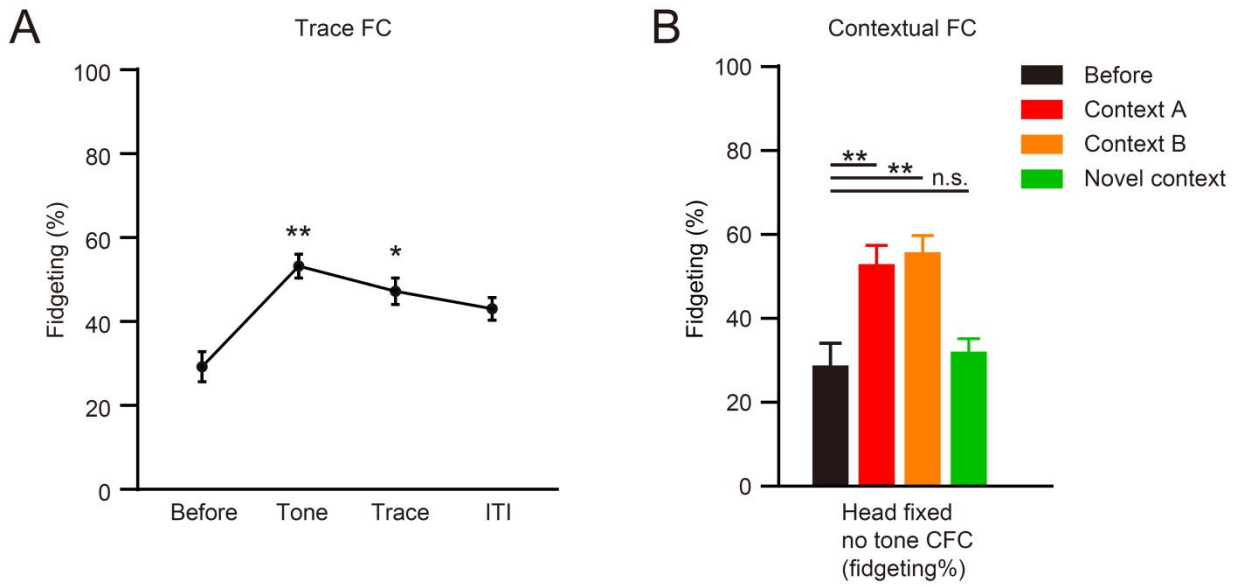

Figure S15. Assessment of paradigm influence on remote memory retrieval. (A) Successful retrieval of remote fear memory upon tone CS presentation. Results were from the same experimental group reported in Fig. 1D in original submission. Tone vs. before, P = 0.008 < 0.01, Trace vs. before, P = 0.023 < 0.05, ITI vs. before, P = 0.120 > 0.05, n = 5 animals. **(B)** Successful retrieval of remote contextual fear memory without tone stimuli under free moving paradigm. Left, freezing response of contextual fear conditioning (CFC) test in free moving conditioning box. Before = 21.00 ± 1.76, Context A = 50.00 ± 2,78, Context B = 52.80 ± 4.44, novel = 23.20 ± 2.25; Context A vs. before, P = < 0.0001, context B vs. before, P < 0.0001, novel vs. before, P = 0.915, n = 5 animals. Right, fidgeting response upon presentation of old context A or old context B. Mice were trained without tone stimuli. Before = 29.00 ± 4.97, Context A = 53.20 ± 4.10, Context B = 56.00 ± 3.61, novel = 32.40 ± 2.60; Context A vs. before, P = 0.0003 < 0.001, context B vs. before, P < 0.0001, novel vs. before, P = 0.935, n = 5 animals.

Supplemental Tables

Figure 1 Subject information summary			
Animal ID	Strain	Number of neurons	Number of unsilenced neurons
1	C57B6J	405	5
2	C57B6J	258	3
3	C57B6J	198	2
4	C57B6J	359	4
5	C57B6J	502	6
6	C57B6J	314	4
7	C57B6J	204	3
8	C57B6J	193	2
9	C57B6J	305	3
10	C57B6J	423	5
11	C57B6J	333	4

Figure 2 Subject information summary				
Animal ID	Strain	Number of neurons	Number of GABAergic neurons	Number of unsilenced neurons
1	GABA:; Ai9	220	24	3
2	GABA:; Ai9	248	32	3
3	GABA:; Ai9	186	17	4
4	GABA:; Ai9	302	29	5
5	GABA:; Ai9	325	37	5
6	GABA:; Ai9	198	35	3
7	GABA:; Ai9	586	114	3

8	GABA:; Ai9	439	53	4
9	GABA:; Ai9	476	69	5
10	GABA:; Ai9	625	103	4
11	GABA:; Ai9	503	96	5

Figure 3 Subjects information summary				
Animal ID	Strain	Number of neurons	Number of high sync. neurons	Number of unsilenced neurons
1	GABA:; Ai9	220	2	2
2	GABA:; Ai9	248	4	3
3	GABA:; Ai9	186	4	4
4	GABA:; Ai9	302	6	5
5	GABA:; Ai9	325	5	5
6	GABA:; Ai9	198	3	3

Figure 5 Two context experiment subjects information summary				
Animal ID	Strain	Number of neurons	Number of unsilenced neurons for context A	Number of unsilenced neurons for context B
1	GABA:; Ai9	118	4	3
2	GABA:; Ai9	263	3	5
3	GABA:; Ai9	194	4	4
4	GABA:; Ai9	220	3	3
5	GABA:; Ai9	251	4	5
6	GABA:; Ai9	252	3	3

Figure 5 3D volumetric imaging subjects information summary			
Animal	Strain	Number of neurons	Number of unsilenced neurons

ID			
1	GABA:; Ai9	985	32
2	GABA:; Ai9	867	25
3	GABA:; Ai9	756	28
4	GABA:; Ai9	1032	31
5	GABA:; Ai9	1135	38

Figure S10 engram subjects information summary			
Animal ID	Strain	Number of neurons	Number of unsilenced neurons
1	GABA:; Ai9	387	4
2	GABA:; Ai9	512	5
3	GABA:; Ai9	399	3
4	GABA:; Ai9	424	6

Figure S12 all two context subjects information summary				
Animal ID	Strain	Number of neurons	Number of unsilenced neurons for context A	Number of unsilenced neurons for context B
1	GABA:; Ai9	510	3	5
2	GABA:; Ai9	437	4	3
3	GABA:; Ai9	405	5	4
4	GABA:; Ai9	248	3	2
5	GABA:; Ai9	351	5	3